

# Chapter 6

## Molecular Magnetism of Metal Complexes and Light-Induced Phase Transitions



Norimichi Kojima and Atsushi Okazawa

**Abstract** One of the most attractive research in the field of molecular solids is multifunctional molecular magnets coupled with spin, charge and photon, and single-molecular magnet/single-chain magnet toward spintronics. In this chapter, we focus on the molecular magnetism and its related light-induced phase transitions from the viewpoint of Mössbauer spectroscopy. In the Sect. 6.1, the outline of this chapter is described. In the Sect. 6.2, static and dynamic spin crossover phenomena between the high-spin and low-spin states, and the spin frustration system induced by dynamic spin crossover phenomena for  $[\text{Mn}^{\text{II}}\text{Fe}^{\text{III}}(\text{C}_2\text{O}_3\text{S})_3]$  complex are described. In the Sect. 6.3, metal complexes showing charge transfer phase transitions such as Prussian blue analogous complexes and  $[\text{Fe}^{\text{II}}\text{Fe}^{\text{III}}(\text{C}_2\text{O}_2\text{S}_2)_3]$  complexes and their photo-induced phase transitions are described. In the Sect. 6.4, various kinds of molecular magnets including single molecular chain magnets are described.

### List of Abbreviations and Symbols

CTPT	Charge transfer phase transition
CTIST	Charge transfer induced spin transition
IVCT	Inter-valence charge transfer
HS	High spin
LS	Low spin
HTP	High temperature phase
LTP	Low temperature phase
<i>IS</i>	Isomer shift
<i>QS</i>	Quadrupole splitting

---

N. Kojima (✉)  
Toyota Physical and Chemical Research Institute, Yokomichi 41-1, Nagakute,  
Aichi 480-1192, Japan  
e-mail: [cnori-kojima@g.ecc.u-tokyo.ac.jp](mailto:cnori-kojima@g.ecc.u-tokyo.ac.jp)

A. Okazawa  
Division of Chemistry, Institute of Liberal Education, Nihon University School of Medicine,  
Oyaguchi Kamimachi 30-1, Itabashi-ku, Tokyo 173-8610, Japan

LIESST	Light induced excited spin state trapping
$T_{CT}$	Critical temperature of charge transfer phase transition
SP	Spiropyran
SMMs	Single-molecule magnets
SCMs	Single-chain magnets
SIMs	Single-ion magnets
QTM	Quantum tunneling of magnetization.

## 6.1 Introduction

Transition-metal complexes consist of transition-metal elements and various kinds of ligands with the ability to control the structural dimensionality, which have produced wide variety of magnetic materials such as low-dimensional magnets, photo-induced magnets, single-molecule magnets (SMMs) and so forth, which have stimulated the theory of molecular magnetism. Thus, the development of advanced magnetic materials and the theory of molecular magnetism have mutually stimulated each other. Especially, the discoveries of light induced excited state spin trapping (LIESST) for spin crossover system (1984), SMM of  $[Mn_{12}]$  cluster complex (1993), and photo-induced ferrimagnet of Prussian blue analogous complex (1996) have significantly expanded the field of molecular magnetism. These recent topics of molecular magnetism are reviewed in the following excellent books [1].

In this chapter, we focus on the molecular magnetism and its related light-induced phase transitions from the viewpoint of Mössbauer spectroscopy. Among various kinds of molecular compounds, in the case of transition-metal complexes whose spin states are situated in the spin crossover region, new types of synergetic phenomena coupled with spin and charge are expected. Based on this viewpoint, we have synthesized organic–inorganic hybrid systems,  $A[Fe^{II}Fe^{III}X_3]$  [ $A = (C_nH_{2n+1})_4N$ , spiropyran, etc.;  $X = dtO (C_2O_2S_2)$ ,  $mto (C_2O_3S)$ ,  $tto (C_2OS_3)$ ] and have found novel multifunctional phenomena coupled with spin, charge and photon [2].

In general, the  $Fe^{III}$  site coordinated by six S atoms is in the low spin (LS) state, while that coordinated by six O atoms is in the high spin (HS) state. Therefore, the spin state of  $Fe^{III}$  coordinated by three S atoms and three O atoms is expected to be situated in the spin crossover region. Based on this viewpoint, we have synthesized  $(C_6H_5)_4P[Zn^{II}Fe^{III}(mto)_3]$  consisting of  $Fe^{III}O_3S_3$  and  $Zn^{II}O_6$  octahedra, and the  $^{57}Fe$  Mössbauer spectroscopy and the electron spin resonance (ESR) revealed the dynamic spin equilibrium phenomenon occurs at the  $Fe^{III}O_3S_3$  site in which the HS and LS states exchange alternately in the time scale of  $10^{-10} < \tau < 10^{-7}$  s [3]. On the other hand, in the case of  $(C_6H_5)_4P[Mn^{II}Fe^{III}(mto)_3]$  consisting of  $Fe^{III}O_3S_3$  and  $Mn^{II}O_6$ , there exists a dynamic spin equilibrium ( $\tau < 10^{-7}$  s) between the HS and LS states at the  $Fe^{III}O_3S_3$  site, which induces the frustration of internal magnetic field between the ferromagnetic and antiferromagnetic interactions at the  $Mn^{II}O_6$  site. Owing to the frustration of internal magnetic field at the  $Mn^{II}$  site caused by

the rapid spin equilibrium at the Fe<sup>III</sup> site, (C<sub>6</sub>H<sub>5</sub>)<sub>4</sub>P[Mn<sup>II</sup>Fe<sup>III</sup>(mto)<sub>3</sub>] undergoes the successive magnetic phase transitions at 30 and 23 K.

In the case of (n-C<sub>n</sub>H<sub>2n+1</sub>)<sub>4</sub>N[Fe<sup>II</sup>Fe<sup>III</sup>(dto)<sub>3</sub>], in addition to the ferromagnetic phase transition, a spin-entropy driven charge transfer phase transition (CTPT) takes place, in which the electrons of Avogadro's constant transfer between the Fe<sup>II</sup> and Fe<sup>III</sup> sites [4]. At the CTPT, the Fe valence state is dynamically fluctuated, which was revealed by means of muon spin relaxation ( $\mu$ SR) [5]. The CTPT and the ferromagnetic phase transition strongly depend on the honeycomb ring size in [Fe<sup>II</sup>Fe<sup>III</sup>(dto)<sub>3</sub>]<sub>∞</sub> [6]. The increase of counter-cation size expands the honeycomb ring, which stabilizes and destabilizes the high temperature phase (HTP) and the low temperature phase (LTP), respectively. In order to control the ferromagnetic properties and the CTPT by means of light irradiation, we have synthesized a photo-responsive organic–inorganic hybrid system, (SP-Me)[Fe<sup>II</sup>Fe<sup>III</sup>(dto)<sub>3</sub>] (SP = spiropyran), and discovered that the photo-isomerization of intercalated SP-Me by UV light irradiation induces the CTPT from the LTP to the HTP in the two-dimensional [Fe<sup>II</sup>Fe<sup>III</sup>(dto)<sub>3</sub>] layer and the change of  $T_C$  from 5 to 22 K, by means of magnetization measurement and <sup>57</sup>Fe Mössbauer spectroscopy [7].

In the Sect. 6.4, we show various kinds of molecular magnets such as SMMs including transition-metal clusters, low-coordinated Fe complexes, and single-chain magnets (SCMs) with easy-plane anisotropy.

## 6.2 Spin Crossover Phenomena

### 6.2.1 Static and Dynamic Spin Crossover Phenomena

Octahedral transition-metal complexes with d<sup>4</sup>–d<sup>7</sup> configurations have a possibility of spin crossover transition between the LS and HS states in the ground state. If the ligand field splitting energy is smaller than the spin-pairing energy in the d orbitals, the d electrons occupy the t<sub>2g</sub> (d<sub>xy</sub>, d<sub>yz</sub>, d<sub>zx</sub>) and the e<sub>g</sub> (d<sub>x<sup>2</sup>-y<sup>2</sup></sub>, d<sub>z<sup>2</sup></sub>) orbitals being followed by Hund's rule, in which the spin configuration shows the maximum spin multiplicity (HS state). On the other hand, if the ligand field splitting energy is larger than the spin-pairing energy, Hund's rule is broken down, in which the spin configuration shows the minimum spin multiplicity (LS state). Therefore, the ground state of the transition metal ion with d<sup>n</sup> (n = 4–7) is ruled by the competition between ligand field splitting energy and spin-pairing energy in the d electrons, which is schematically shown in Fig. 6.1.

The energy diagram for d<sup>n</sup> system called Tanabe–Sugano diagram is the most effective tool to analyze the competition between the HS and LS states as the ground state [8]. The Tanabe–Sugano diagram exhibits the energies of multiplets for 3d<sup>n</sup> (n = 2–8) system as a function of the ratio of ligand field ( $Dq$ ) to the Racah parameter ( $B$ ) representing the strength of Coulomb interaction between 3d electrons. In the case of 3d<sup>n</sup> (n = 4–7), if the ground energies of HS and LS states are close to each

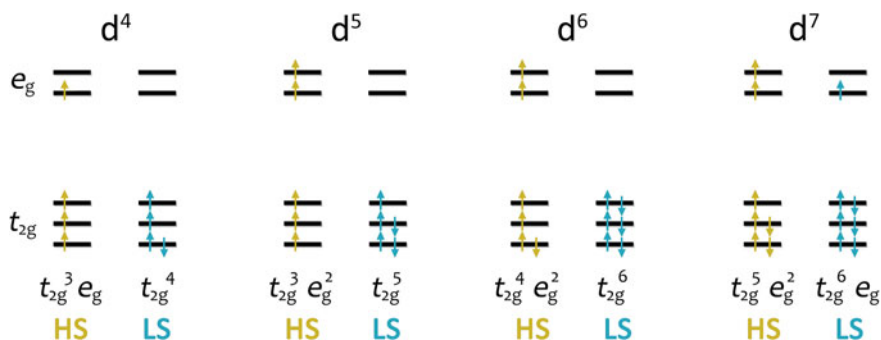
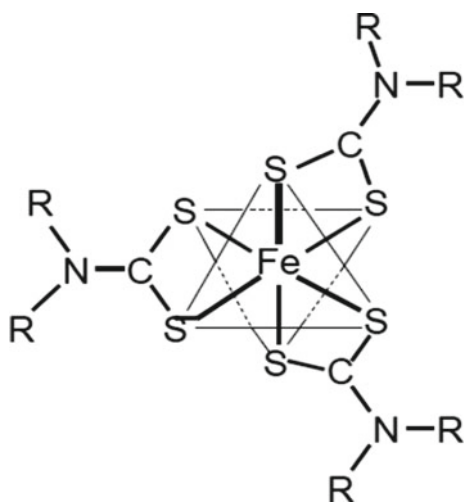


**Fig. 6.1** Spin arrangements in the ground states for  $d^n$  ( $n = 4-7$ ) configuration with octahedral symmetry

other, the system has a possibility to convert the spin states between the HS and LS states by external perturbations such as heat, applied pressure or light irradiation. Such the HS–LS conversion is called spin crossover phenomenon.

The spin crossover phenomenon was observed for the first time by L. Cambi et al. in 1930s for tris(dithiocarbamato)iron(III) complexes,  $\text{Fe}^{\text{III}}(\text{S}_2\text{CNR}_2)_3$  ( $R = n\text{-C}_4\text{H}_9$ ,  $iso\text{-C}_4\text{H}_9$ , etc.) [9]. In this system, as shown in Fig. 6.2, the  $\text{Fe}^{\text{III}}$  ion is coordinated by six S atoms. According to L. Cambi et al., the magnetic susceptibilities of  $\text{Fe}^{\text{III}}(\text{S}_2\text{CNR}_2)_3$  significantly change depending on temperature caused by the gradual LS ( $S = 1/2$ )–HS ( $S = 5/2$ ) transition, which is shown in Fig. 6.3. If the spin conversion between the LS ( $S = 1/2$ ) and HS ( $S = 5/2$ ) states is slower than the time scale ( $\tau = 10^{-7}$  s) of  $^{57}\text{Fe}$  Mössbauer spectroscopy, two kinds of quadrupole doublets corresponding to the HS and LS states should be clearly distinguished. On the other hand, if the spin conversion is faster than  $10^{-7}$  s, an averaged quadrupole doublet

**Fig. 6.2** Molecular structure of  $\text{Fe}^{\text{III}}(\text{S}_2\text{CNR}_2)_3$  ( $R = n\text{-C}_n\text{H}_{2n+1}$ , etc.)



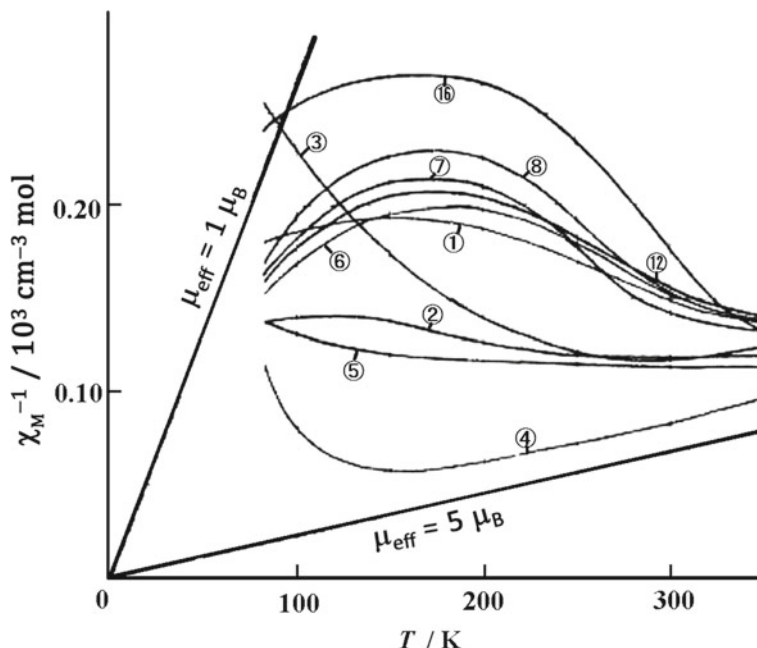


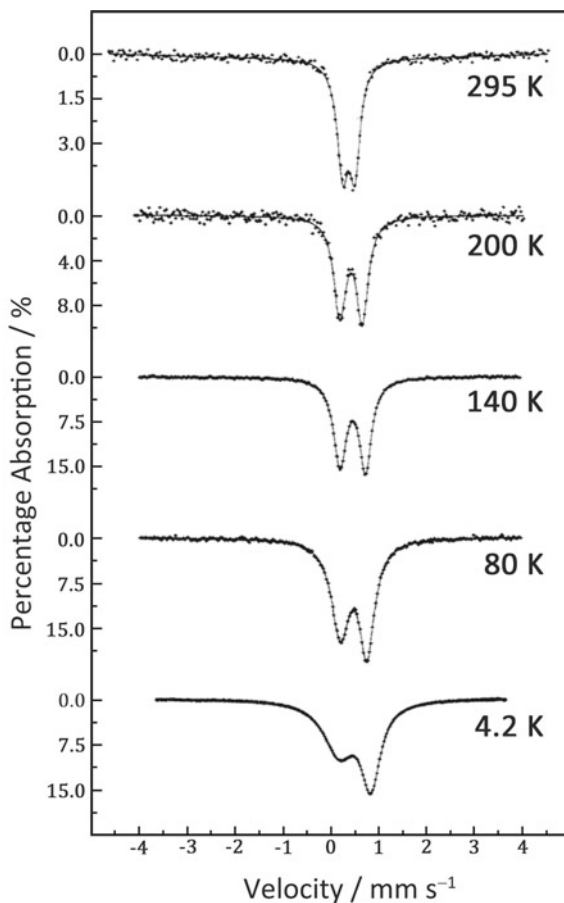
**Fig. 6.3** Inverse magnetic susceptibilities as a function of temperature for  $\text{Fe}^{\text{III}}(\text{S}_2\text{CNR}_2)_3$  ( $R = n\text{-C}_n\text{H}_{2n+1}$ , etc.). (Reprinted from [9(c)]. Copyright Wiley-VCH Verlag GmbH & Co. KGaA)

should be observed. In the case of  $\text{Fe}^{\text{III}}(\text{S}_2\text{CNR}_2)_3$  ( $R = \text{C}_2\text{H}_5$ ), as shown in Fig. 6.4, the  $^{57}\text{Fe}$  Mössbauer spectrum exhibits a broad quadrupole doublet in the temperature range of the gradual LS ( $S = 1/2$ )  $\leftrightarrow$  HS ( $S = 5/2$ ) transition, which shows that the rapid spin equilibrium between the HS and LS states is realized in the time scale of  $\tau < 10^{-7}$  s [10]. Until now, various kinds of  $\text{Fe}^{\text{III}}$  complexes consisting of  $\text{Fe}^{\text{III}}\text{S}_6$ ,  $\text{Fe}^{\text{III}}\text{O}_3\text{S}_3$ , or  $\text{Fe}^{\text{III}}\text{N}_4\text{O}_2$  octahedra exhibiting rapid spin equilibrium phenomena have been reported [11].

Thirty years after the discovery of spin-crossover phenomenon for  $\text{Fe}^{\text{III}}(\text{S}_2\text{CNR}_2)_3$ , W.A. Baker et al. reported the spin-crossover phase transition for  $[\text{Fe}^{\text{II}}(\text{phen})_2\text{X}_2]$  (phen = 1,10-phenanthroline, X = NCS or NCS<sub>e</sub>) [12]. In  $[\text{Fe}^{\text{II}}(\text{phen})_2(\text{NCS})_2]$ , the  $\text{Fe}^{\text{II}}$  ion is coordinated by six N atoms of phen and NCS molecules, and this complex undergoes the first-order LS ( $^1\text{A}_{1g}$ ,  $S = 0$ )–HS ( $^5\text{T}_{2g}$ ,  $S = 2$ ) transition at 176 K with a small thermal hysteresis. Since the discovery of the spin-crossover phase transition for  $[\text{Fe}^{\text{II}}(\text{phen})_2\text{X}_2]$  (X = NCS, NCS<sub>e</sub>), various kinds of spin crossover complexes have been reported for  $\text{Cr}^{\text{II}}$  ( $3d^4$ ),  $\text{Mn}^{\text{III}}$  ( $3d^4$ ),  $\text{Mn}^{\text{II}}$  ( $3d^5$ ),  $\text{Fe}^{\text{III}}$  ( $3d^5$ ),  $\text{Fe}^{\text{II}}$  ( $3d^6$ ),  $\text{Co}^{\text{III}}$  ( $3d^6$ ), and  $\text{Co}^{\text{II}}$  ( $3d^7$ ) complexes [13–15], in which most of them are  $\text{Fe}^{\text{II}}$  ( $3d^6$ ) and  $\text{Fe}^{\text{III}}$  ( $3d^5$ ) complexes.

The spin-crossover phenomena have attracted much attention since the discovery of the light-induced spin transition for  $[\text{Fe}^{\text{II}}(\text{ptz})_6](\text{BF}_4)_2$  (ptz = 1-propyltetrazole) in 1984 [16(b)]. This complex exhibits a sharp spin transition at 135 K with a remarkable

**Fig. 6.4**  $^{57}\text{Fe}$  Mössbauer spectra of  $\text{Fe}^{\text{III}}(\text{S}_2\text{CNR}_2)_3$  ( $\text{R} = \text{C}_2\text{H}_5$ ) at various temperatures. Reprinted with permission from [10]. Copyright 1987 American Chemical Society



change of color [16(a)]. The color in the LS state is purple, while that in the HS state is colorless. S. Decurtins, P. Güthlich, et al. discovered a persistent light-induced HS state for  $[\text{Fe}^{\text{II}}(\text{ptz})_6](\text{BF}_4)_2$  when they measured the optical absorption spectra at 8 K with white light including the spin-allowed absorption region ( $^1\text{A}_{1g}(\text{t}_{2g}^6) \rightarrow ^1\text{T}_{1g}, ^1\text{T}_{2g}(\text{t}_{2g}^5\text{e}_g)$  transitions), in which the purple color was completely “bleached” and the colorless remained unchanged as long as the temperature was kept below 50 K [16(c)]. This light-induced spin-crossover phenomenon was named LIESST (Light Induced Excited Spin State Trapping) by them. The trapping  $^5\text{T}_{2g}$  state of the lowest HS state could also be optically pumped back to the  $^1\text{A}_{1g}$  ground state via intermediate triplet states  $^3\text{T}_{1g}, ^3\text{T}_{2g}(\text{t}_{2g}^5\text{e}_g)$  by the light irradiation corresponding to the  $^5\text{T}_{2g} \rightarrow ^5\text{E}_g$  transition, which was called reverse-LIESST. The discovery of LIESST and reverse-LIESST have attracted much attention from the viewpoint of photonic molecular devices, and various kinds of spin crossover complexes showing LIESST have been developed mainly for  $\text{Fe}^{\text{II}}$  and  $\text{Fe}^{\text{III}}$  complexes [17]. Figure 6.5

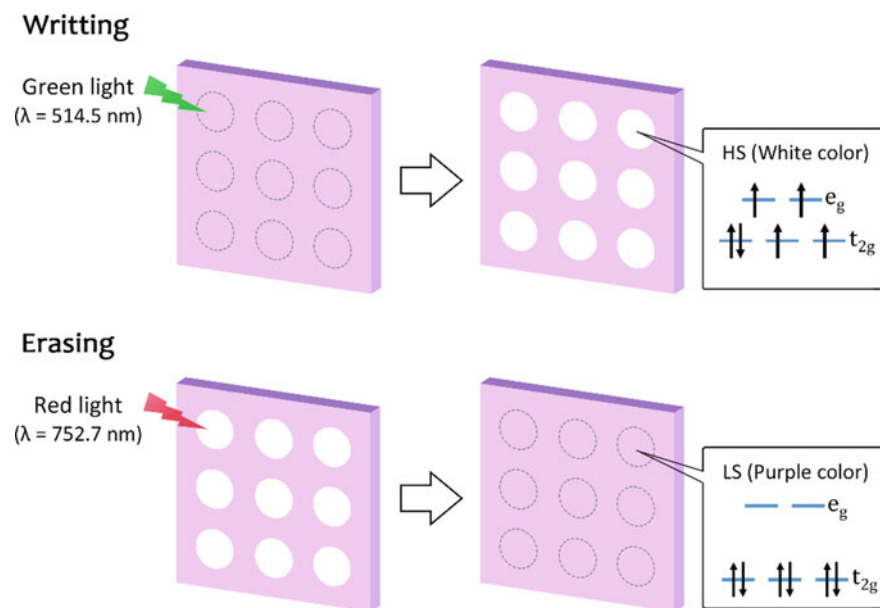


**Fig. 6.5** Schematic demonstration of the erasable optical recording based on the LIESST and reverse-LIESST for  $[\text{Fe}^{\text{II}}(\text{ptz})_6](\text{BF}_4)_2$

shows the schematic demonstration of the erasable optical recording based on the LIESST and reverse-LIESST for  $[\text{Fe}^{\text{II}}(\text{ptz})_6](\text{BF}_4)_2$ .

### 6.2.2 Dynamic Spin Crossover Phenomena of $A[M^{\text{II}}\text{Fe}^{\text{III}}(\text{mto})_3]$ ( $A = \text{Counter Cation}; M = \text{Zn}, \text{Cd}; \text{mto} = \text{C}_2\text{O}_3\text{S}$ )

In this section, we focus on the spin crossover phenomenon of  $\text{Fe}^{\text{III}}$  coordinated by three S atoms and three O atoms,  $\text{Fe}^{\text{III}}\text{O}_3\text{S}_3$ . In general, the  $\text{Fe}^{\text{III}}$  site coordinated by six S atoms tends to be in the LS state ( $t_{2g}^5$ ,  $S = 1/2$ ), while the  $\text{Fe}^{\text{III}}$  site coordinated by six O atoms is in the HS state ( $t_{2g}^3e_g^2$ ,  $S = 5/2$ ). Therefore, the spin state of  $\text{Fe}^{\text{III}}\text{O}_3\text{S}_3$  has a possibility to exhibit the spin-crossover phenomenon between the LS and HS states, which is schematically shown in Fig. 6.6.

As a matter of fact, in the case of tris(monothio- $\beta$ -diketonato)iron(III) complexes, the LS ( $S = 1/2$ ) and HS ( $S = 5/2$ ) states coexist between 300 and 80 K, and two kinds of quadrupole doublets corresponding to the LS and HS states are clearly distinguished in the  $^{57}\text{Fe}$  Mössbauer spectra, in which the component of LS state increases with decreasing temperature from 300 to 80 K [18]. In the case of

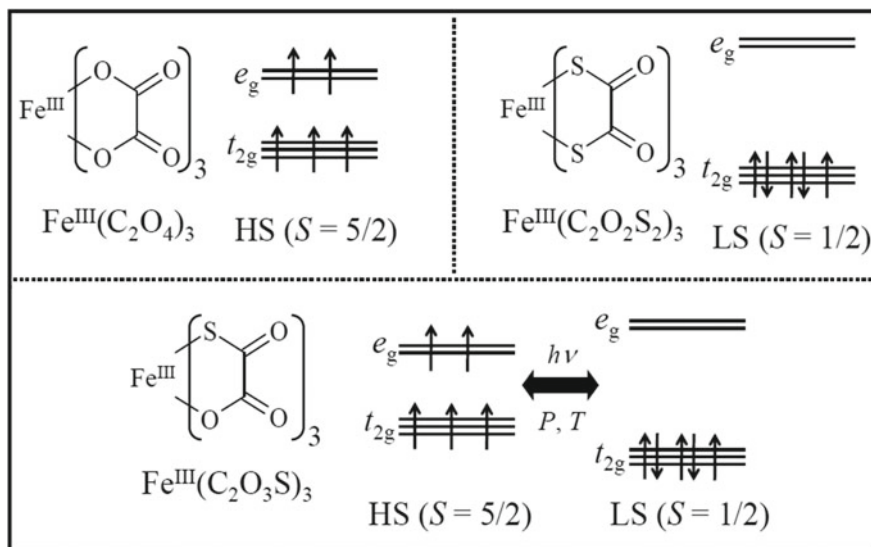


**Fig. 6.6** Spin states of the  $\text{Fe}^{\text{III}}$  sites for  $[\text{Fe}^{\text{III}}(\text{ox})_3]$ ,  $[\text{Fe}^{\text{III}}(\text{dto})_3]$ , and  $[\text{Fe}^{\text{III}}(\text{mto})_3]$

tris(monothiocarbamato)iron(III) complexes, on the other hand, the rapid spin equilibrium occurs in which the HS and LS states exchange in the time scale of less than  $10^{-7}$  s [19]. In this case, an averaged quadrupole doublet between the HS and LS states is observed. However, the rapid spin equilibrium phenomenon has not yet been found for assembled metal complex systems. For this viewpoint, in order to search the rapid spin equilibrium phenomenon for assembled metal complex system including  $\text{Fe}^{\text{III}}\text{O}_3\text{S}_3$  site, we have synthesized  $(\text{C}_6\text{H}_5)_4\text{P}[\text{M}^{\text{II}}\text{Fe}^{\text{III}}(\text{mto})_3]$  ( $\text{M} = \text{Mn}, \text{Zn}$ ) consisting of the  $\text{Fe}^{\text{III}}\text{O}_3\text{S}_3$  and  $\text{M}^{\text{II}}\text{O}_6$  sites and investigated the spin state of the  $\text{Fe}^{\text{III}}\text{O}_3\text{S}_3$  site [3].

Based on the crystal structure of  $(n\text{-C}_3\text{H}_7)_4\text{N}[\text{Fe}^{\text{II}}\text{Fe}^{\text{III}}(\text{dto})_3]$  analyzed by the single-crystal X-ray diffraction [20], the Rietveld analysis was performed for the powder X-ray diffraction pattern of  $(\text{C}_6\text{H}_5)_4\text{P}[\text{Mn}^{\text{II}}\text{Fe}^{\text{III}}(\text{mto})_3]$  at room temperature. In this complex, the  $\text{Mn}^{\text{II}}$  and  $\text{Fe}^{\text{III}}$  ions are alternately arrayed by the bridging ligand, mto, which forms the honeycomb network structure of  $[\text{Mn}^{\text{II}}\text{Fe}^{\text{III}}(\text{mto})_3]$ . The  $(\text{C}_6\text{H}_5)_4\text{P}^+$  layer is intercalated between two adjacent  $[\text{Mn}^{\text{II}}\text{Fe}^{\text{III}}(\text{mto})_3]$  layers.

In the case of  $(n\text{-C}_4\text{H}_9)_4\text{N}[\text{Zn}^{\text{II}}\text{Fe}^{\text{III}}(\text{ox})_3]$  with a similar structure of  $(\text{C}_6\text{H}_5)_4\text{P}[\text{Zn}^{\text{II}}\text{Fe}^{\text{III}}(\text{mto})_3]$ , the  $\chi T$  value ( $= 4.22 \text{ cm}^3 \text{ K mol}^{-1}$ ) is almost constant between 300 and 4.2 K, whose value is regarded as the spin-only  $\chi T$  value ( $4.375 \text{ cm}^3 \text{ K mol}^{-1}$ ) of the HS state ( $S = 5/2$ ) for  $\text{Fe}^{\text{III}}$  [21]. On the other hand, the  $\chi T$  value for  $(\text{C}_6\text{H}_5)_4\text{P}[\text{Zn}^{\text{II}}\text{Fe}^{\text{III}}(\text{mto})_3]$  decreases from 3.60 (at 300 K) to  $2.66 \text{ cm}^3 \text{ K mol}^{-1}$  (at 4.2 K) [3]. Therefore, the  $\chi T$  value of  $(\text{C}_6\text{H}_5)_4\text{P}[\text{Zn}^{\text{II}}\text{Fe}^{\text{III}}(\text{mto})_3]$  is considered to be situated in the middle value between those of the HS and LS states for  $\text{Fe}^{\text{III}}$ .

Figure 6.7a shows the X-band ESR spectra for  $(\text{C}_6\text{H}_5)_4\text{P}[\text{Zn}^{\text{II}}\text{Fe}^{\text{III}}(\text{mto})_3]$  at 300, 77 and 10 K, in which the ESR signals corresponding to the HS and LS states



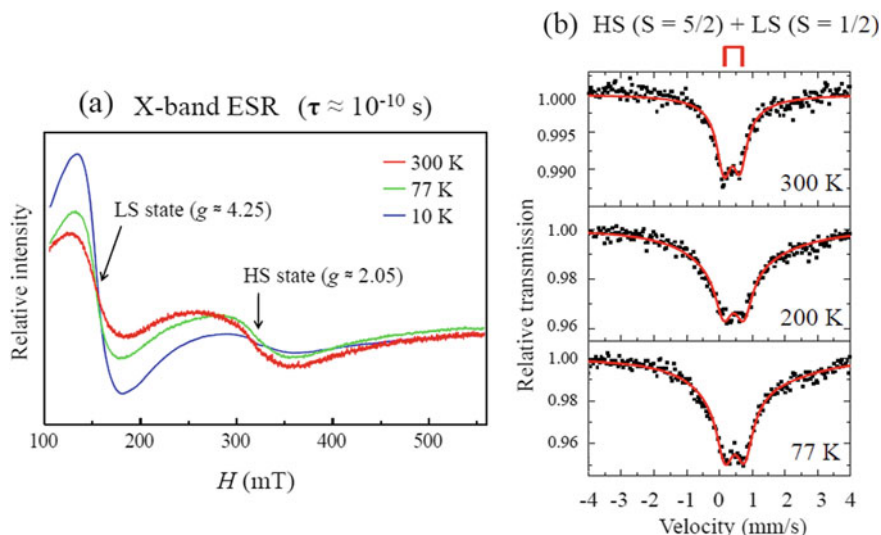


**Fig. 6.7** a X-band ESR spectra, and b  $^{57}\text{Fe}$  Mössbauer spectra for  $(\text{C}_6\text{H}_5)_4\text{P}[\text{Zn}^{\text{II}}\text{Fe}^{\text{III}}(\text{mto})_3]$  at various temperatures. Reprinted with permission from [3]. Copyright 2010 the Chemical Society of Japan

of  $\text{Fe}^{\text{III}}$  site are clearly distinguished at about 300 mT ( $g \approx 2.05$ ) and 150 mT ( $g \approx 4.25$ ), respectively. The ESR intensity ratio of the LS state to the HS state increases with decreasing temperature, which is consistent with the temperature dependence of  $\chi_{\text{M}}T$ . Therefore, these results imply that the spin state of  $\text{Fe}^{\text{III}}\text{O}_3\text{S}_3$  in  $(\text{C}_6\text{H}_5)_4\text{P}[\text{Zn}^{\text{II}}\text{Fe}^{\text{III}}(\text{mto})_3]$  is the spin equilibrium between the HS and LS states, and the HS and LS states are clearly distinguished under the time scale ( $10^{-10}$  s) of X-band ESR spectroscopy. Figure 6.7b shows the  $^{57}\text{Fe}$  Mössbauer spectra of  $(\text{C}_6\text{H}_5)_4\text{P}[\text{Zn}^{\text{II}}\text{Fe}^{\text{III}}(\text{mto})_3]$  at 300, 77 and 10 K, where only one quadrupole doublet of  $\text{Fe}^{\text{III}}$  appears in spite of the coexistence of HS and LS states in the ESR signal between 300 and 10 K. Therefore, the  $^{57}\text{Fe}$  Mössbauer spectra of  $(\text{C}_6\text{H}_5)_4\text{P}[\text{Zn}^{\text{II}}\text{Fe}^{\text{III}}(\text{mto})_3]$  indicates the rapid spin equilibrium at the  $\text{Fe}^{\text{III}}$  site whose time scale is faster than that ( $10^{-7}$  s) of the  $^{57}\text{Fe}$  Mössbauer spectroscopy. The relaxation process between the HS and LS states at the  $\text{Fe}^{\text{III}}\text{O}_3\text{S}_3$  site is considered to be a tunneling process. The time scale of spin equilibrium at the  $\text{Fe}^{\text{III}}$  site in  $(\text{C}_6\text{H}_5)_4\text{P}[\text{Zn}^{\text{II}}\text{Fe}^{\text{III}}(\text{mto})_3]$  is estimated at  $10^{-10} < \tau < 10^{-7}$  s. The tunneling probability for a non-radiative multi-phonon process from a given vibrational levels,  $m$  of the HS state and  $m'$  of the LS state is given by the following equation [22],

$$W_{mm'} = \frac{2\pi}{\hbar^2\omega} \beta_{\text{HL}}^2 |\langle \chi_{m'} | \chi_m \rangle|^2 \delta(E_{m'}, E_m), \quad (6.1)$$

where the electronic coupling matrix element  $\beta_{\text{HL}} = \langle \psi_{\text{LS}} | H_{\text{SO}} | \psi_{\text{HS}} \rangle$  is the second order spin-orbit coupling,  $\hbar\omega$  is the energy of metal-ligand vibration,  $\delta(E_{m'}, E_m)$  is

the delta function ensuring energy conservation,  $|\langle \chi_{m'} | \chi_m \rangle|^2$  is the Franck–Condon factor of the overlap of the vibrational functions between the HS state ( $\chi_m$ ) and LS state ( $\chi_{m'}$ ). At  $T \approx 0$  K, since the vibrational ground state of the HS state is populated, the relaxation rate constant between the HS and LS states is expressed as follows [22],

$$k_{\text{HL}}(T \approx 0) = \frac{2\pi}{\hbar^2 \omega} \beta_{\text{HL}}^2 |\langle \chi_n | \chi_0 \rangle|^2, \quad n = \frac{\Delta E_{\text{HL}}^0}{\hbar \omega}, \quad (6.2)$$

where  $|\langle \chi_n | \chi_0 \rangle|^2$  is expressed as follows,

$$|\langle \chi_n | \chi_0 \rangle|^2 = \frac{S^n e^{-S}}{n!}, \quad S = \frac{\frac{1}{2} f \Delta Q_{\text{HL}}^2}{\hbar \omega}, \quad (6.3)$$

where  $S$  is the Huang–Rhys factor [23],  $\Delta Q_{\text{HL}}$  is the difference of horizontal displacement between the HS and LS potential wells in the metal–ligand coordinate geometry, and  $f$  is the force constant. According to Eqs. (6.2) and (6.3), with decreasing the Huang–Rhys factor, the Frank–Condon factor increases, which increases the relaxation rate constant between the HS and LS states. In general, the  $\Delta Q_{\text{HL}}$  of spin crossover  $\text{Fe}^{\text{III}}$  complex is shorter than that of  $\text{Fe}^{\text{II}}$  complex. Indeed, the change in the  $\text{Fe}^{\text{II}}$ –ligand distance due to the HS–LS transition is 0.16–0.21 Å, while that in the  $\text{Fe}^{\text{III}}$ –ligand distance is about 0.12 Å [24], which is the reason why the rapid spin equilibrium phenomenon has been found for  $\text{Fe}^{\text{III}}$  complexes consisting of  $\text{Fe}^{\text{III}}\text{S}_6$ ,  $\text{Fe}^{\text{III}}\text{O}_3\text{S}_3$ , or  $\text{Fe}^{\text{III}}\text{N}_4\text{O}_2$  octahedra.

### 6.2.3 Spin Frustration Induced by Dynamic Spin Crossover Phenomena for $A[\text{Mn}^{\text{II}}\text{Fe}^{\text{III}}(\text{mto})_3]$

In the case of mto bridged hetero-metal complex system,  $[\text{Mn}^{\text{II}}\text{Fe}^{\text{III}}(\text{mto})_3]$  consisting of  $\text{Mn}^{\text{II}}\text{O}_6$  and  $\text{Fe}^{\text{III}}\text{O}_3\text{S}_3$  octahedra, the spin states of the  $\text{Mn}^{\text{II}}$  and  $\text{Fe}^{\text{III}}$  sites are considered to be HS state ( $S = 5/2$ ) and the spin equilibrium state of HS ( $S = 5/2$ )  $\leftrightarrow$  LS ( $S = 1/2$ ), respectively. If the spin state of  $\text{Fe}^{\text{III}}$  site is LS state ( $S = 1/2$ ), there exist four potential exchange interactions ( $J_{\text{P}}$ ) and one kinetic exchange interaction ( $J_{\text{K}}$ ) between the  $\text{Fe}^{\text{III}}$  and  $\text{Mn}^{\text{II}}$  sites. The sum of the potential exchange interaction is considered to be stronger than the kinetic exchange interaction, which is responsible for the ferromagnetic ordering. In connection with this, the following should be mentioned. The ferromagnetic ordering of  $(n\text{-C}_3\text{H}_7)_4\text{N}[\text{Mn}^{\text{II}}\text{Fe}^{\text{III}}(\text{dto})_3]$  with  $\text{Mn}^{\text{II}}$  ( $S = 5/2$ ) and  $\text{Fe}^{\text{III}}$  ( $S = 1/2$ ) has been reported [25], in which the Curie temperature ( $T_{\text{C}}$ ) and the Weiss temperature ( $\theta$ ) were estimated at 4 and 10 K, respectively, from the analysis of magnetization and magnetic susceptibility. On the other hand, if the spin state of  $\text{Fe}^{\text{III}}$  site is HS state ( $S = 5/2$ ), there exist five  $J_{\text{K}}$  between the  $\text{Fe}^{\text{III}}$  and  $\text{Mn}^{\text{II}}$  sites, which are considered to be stronger than the potential exchange interactions between the  $\text{Fe}^{\text{III}}$  and  $\text{Mn}^{\text{II}}$  sites. Indeed, the ferrimagnetic ordering of

$(n\text{-C}_n\text{H}_{2n+1})_4\text{N}[\text{Mn}^{\text{II}}\text{Fe}^{\text{III}}(\text{ox})_3]$  with  $\text{Mn}^{\text{II}}$  ( $S = 5/2$ ) and  $\text{Fe}^{\text{III}}$  ( $S = 5/2$ ) has been reported [26], in which  $T_{\text{N}}$  was estimated at 27–28 K.

Therefore, if the spin state of the  $\text{Fe}^{\text{III}}$  site in the  $[\text{Mn}^{\text{II}}\text{Fe}^{\text{III}}(\text{mto})_3]$  system behaves as the dynamic spin equilibrium phenomenon, the internal magnetic field at the  $\text{Mn}^{\text{II}}$  site should be frustrated between the ferromagnetic and antiferromagnetic interactions, which is schematically shown in Fig. 6.8.

Based on this viewpoint, we have synthesized  $(\text{C}_6\text{H}_5)_4\text{P}[\text{Mn}^{\text{II}}\text{Fe}^{\text{III}}(\text{mto})_3]$  and investigated the magnetic properties [27]. Figure 6.9 shows the temperature dependence of the magnetization and ac magnetic susceptibility for  $(\text{C}_6\text{H}_5)_4\text{P}[\text{Mn}^{\text{II}}\text{Fe}^{\text{III}}(\text{mto})_3]$ . As shown in Fig. 6.9a, with decreasing temperature, the field cooled magnetization (FCM) remarkably increases just below 30 K, then slightly increases below 23 K. In the heating process, the remnant magnetization (RM) disappears at 30 K. On the other hand, both of the real ( $\chi'$ ) and imaginary ( $\chi''$ ) parts of ac magnetic susceptibility exhibit a steep peak at 23 K indicating a magnetic phase transition, which is shown in Fig. 6.9b, c. Therefore, it is obvious that  $(\text{C}_6\text{H}_5)_4\text{P}[\text{Mn}^{\text{II}}\text{Fe}^{\text{III}}(\text{mto})_3]$  undergoes two successive magnetic phase transitions at 30 and 23 K. As shown in Fig. 6.10, the  $^{57}\text{Fe}$  Mössbauer spectra of  $(\text{C}_6\text{H}_5)_4\text{P}[\text{Mn}^{\text{II}}\text{Fe}^{\text{III}}(\text{mto})_3]$  imply that the spin state at the  $\text{Fe}^{\text{III}}$  site is still paramagnetic between 30 and 24 K. Then, both of the  $\text{Mn}^{\text{II}}$  and  $\text{Fe}^{\text{III}}$  spins are eventually ordered at 23 K. In this manner, it is concluded that the successive magnetic phase

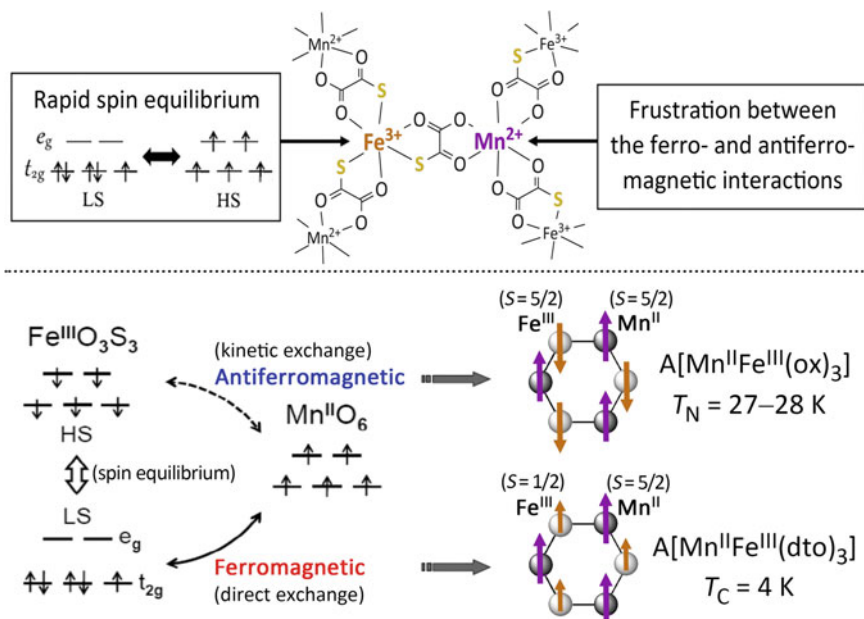
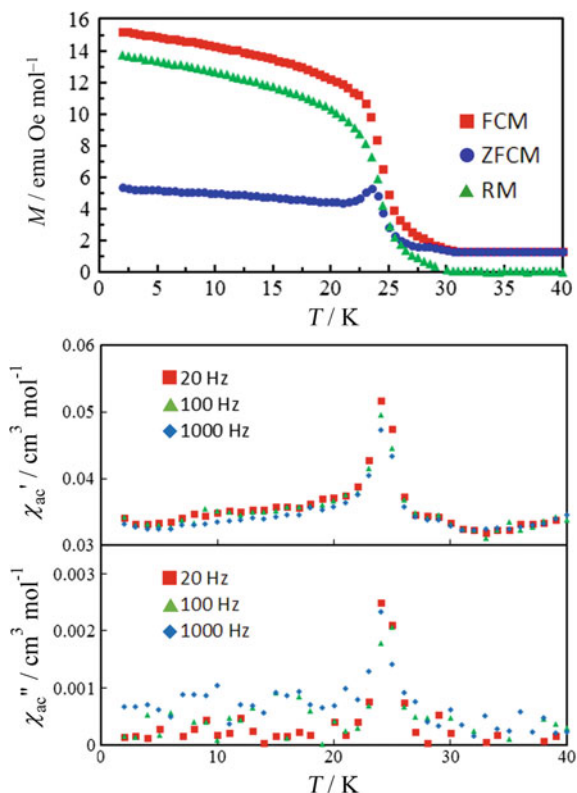


**Fig. 6.8** Schematic representation of the relationship between the rapid spin equilibrium of the  $\text{Fe}^{\text{III}}$  site and the dynamic frustration of internal magnetic field at the  $\text{Mn}^{\text{II}}$  site in  $[\text{Mn}^{\text{II}}\text{Fe}^{\text{III}}(\text{mto})_3]$

**Fig. 6.9** **a** Magnetization, **b** in-phase ac magnetic susceptibility ( $\chi'$ ), and **c** out-phase ac magnetic susceptibility ( $\chi''$ ) of  $(\text{C}_6\text{H}_5)_4\text{P}[\text{Mn}^{\text{II}}\text{Fe}^{\text{III}}(\text{mto})_3]$  as a function of temperature. FCM: field-cooled magnetization, ZFCM: zero-field-cooled magnetization, RM: remnant magnetization. FCM and ZFCM were measured at 3.0 mT. The ac magnetic susceptibility measurements were performed under the ac magnetic field of 0.3 mT and the frequency between 20 and 1000 Hz



transitions at 30 and 23 K for  $(\text{C}_6\text{H}_5)_4\text{P}[\text{Mn}^{\text{II}}\text{Fe}^{\text{III}}(\text{mto})_3]$  are induced by the rapid spin equilibrium at the  $\text{Fe}^{\text{III}}$  site.

Taking account of the temperature dependences of the magnetization, ac magnetic susceptibility, and  $^{57}\text{Fe}$  Mössbauer spectra for  $(\text{C}_6\text{H}_5)_4\text{P}[\text{Mn}^{\text{II}}\text{Fe}^{\text{III}}(\text{mto})_3]$ , the Gibbs energies of the A, B and C phases as a function of temperature for  $(\text{C}_6\text{H}_5)_4\text{P}[\text{Mn}^{\text{II}}\text{Fe}^{\text{III}}(\text{mto})_3]$  are schematically represented in Fig. 6.11, in which the A, B and C phases are defined as follows,

Phase A The spins at the  $\text{Mn}^{\text{II}}$  and  $\text{Fe}^{\text{III}}$  sites are paramagnetic.

Phase B The spin at the  $\text{Mn}^{\text{II}}$  site is ordered, while that at the  $\text{Fe}^{\text{III}}$  site is still paramagnetic.

Phase C Both of the spins at the  $\text{Mn}^{\text{II}}$  and  $\text{Fe}^{\text{III}}$  sites are ordered.

As shown in Fig. 6.11, with decreasing temperature, the first magnetic phase transition from the phase A to the phase B takes place at 30 K, then the second magnetic phase transition from the phase B to the phase C takes place at 23 K.

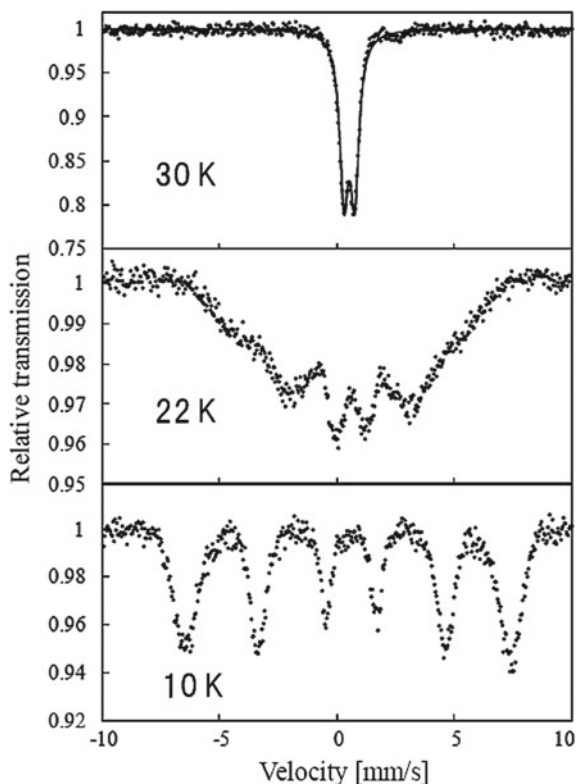


Fig. 6.10  $^{57}\text{Fe}$  Mössbauer spectra of  $(\text{C}_6\text{H}_5)_4\text{P}[\text{Mn}^{\text{II}}\text{Fe}^{\text{III}}(\text{mto})_3]$  at 30, 22 and 10 K

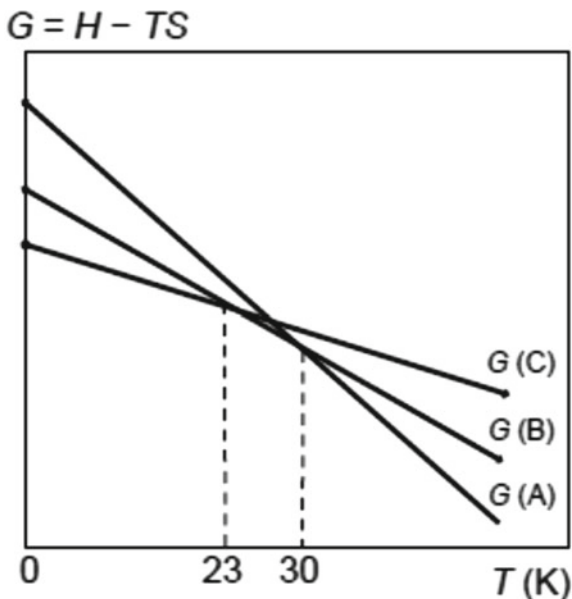
## 6.3 Mixed-Valence System and Charger Transfer Phase Transition

### 6.3.1 Classification of Mixed-Valence System

Mixed-valence compounds, defined as compounds containing an element with more than one oxidation state, are classified into three groups according to the Robin–Day classification [28],

- Class I      Compounds whose valence states occupy different crystallographic sites and are too distant from each other to allow the electronic interaction between the mixed-valence states.
- Class II     Compounds in which an electron exchange between the different valence states takes place as a thermally activated process. The intervalence charge transfer (IVCT) between different valence states is observable in optical absorption spectra.

**Fig. 6.11** Schematic Gibbs energies of the A, B and C phases as a function of temperature for  $(C_6H_5)_4P[Mn^{II}Fe^{III}(mto)_3]$ .  $G(A)$ ,  $G(B)$  and  $G(C)$  indicate the Gibbs energies for the A, B and C phases, respectively. Phase A: The spins at the  $Mn^{II}$  and  $Fe^{III}$  sites are paramagnetic, Phase B: The spin at the  $Mn^{II}$  site is ordered, while that at the  $Fe^{III}$  site is still paramagnetic, Phase C: Both of the spins at the  $Mn^{II}$  and  $Fe^{III}$  sites are ordered



Class III(A) Compounds in which valence electrons are delocalized between atoms within discrete polynuclear ions.

Class III(B) Compounds in which valence electrons are delocalized between identically crystallographic sites.

### 6.3.2 Prussian Blue and Its Analogues Salts Showing Photo-Induced Magnetism

Among these mixed-valence compounds, the boundary compounds between the class II and III are the leading candidates exhibiting field-responsive multifunctional properties coupled with transport, optical or magnetic properties. In this section, we describe the characteristic properties of Prussian blue and its analogous compounds as an example.

Prussian blue has a three dimensional network structure with an alternating array of  $Fe^{II}$  and  $Fe^{III}$  ions through CN bridges [29], which is schematically shown in Fig. 6.12a. The spin state of the  $Fe^{II}$  site coordinated by six C atoms is LS ( $S = 0$ ) state, and that of the  $Fe^{III}$  site coordinated by six N atoms is HS ( $S = 5/2$ ) state. Prussian blue has a broad strong IVCT band at around 730 nm, which is responsible for the deep blue pigment. Figure 6.12b shows “The Great Wave off Kanagawa” painted by Hokusai, in which Prussian blue was used as a deep blue pigment.

The soluble Prussian blue,  $KFe^{II}Fe^{III}(CN)_6$ , is obtained by adding  $Fe^{3+}$  to the aqueous solution of  $K_4[Fe^{II}(CN)_6]$ , as following scheme,  $Fe^{3+}(aq) + K^+(aq) + [Fe^{II}(CN)_6]^{4-}(aq) \rightarrow KFe^{II}Fe^{III}(CN)_6(s)$ . On the other hand, by adding  $Fe^{2+}$  to the

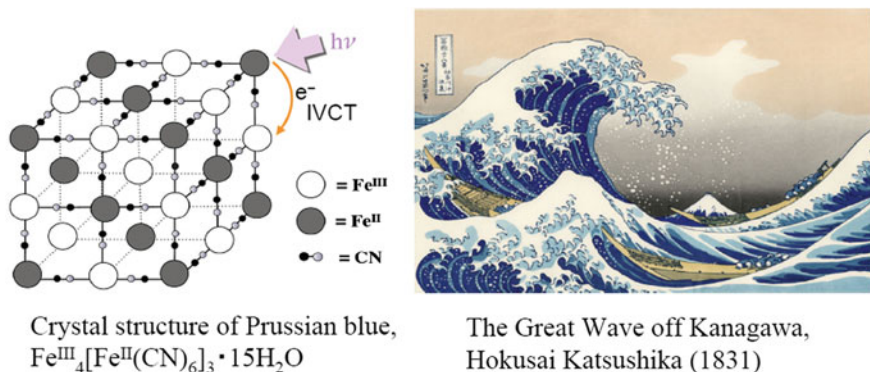


**Fig. 6.12** **a** Schematic representation of the crystal structure of  $\text{Fe}_4^{\text{III}}[\text{Fe}^{\text{II}}(\text{CN})_6]_3$ , **b** “The Great Wave off Kanagawa” painted by Hokusai, in which Prussian blue was used as deep blue pigment

aqueous solution of  $\text{K}_3[\text{Fe}^{\text{III}}(\text{CN})_6]$ ,  $\text{KFe}^{\text{II}}\text{Fe}^{\text{III}}(\text{CN})_6$  called Turnbull’s blue is also obtained as follows,  $\text{Fe}^{2+}(\text{aq}) + \text{K}^+(\text{aq}) + [\text{Fe}^{\text{III}}(\text{CN})_6]^{3-}(\text{aq}) \rightarrow \text{KFe}^{\text{II}}\text{Fe}^{\text{III}}(\text{CN})_6(\text{s})$ . A long historical debate had continued in relation to Prussian blue and Turnbull’s blue, whether Prussian blue obtained by mixing the solutions of ferric compound and ferrocyanide, and Turnbull’s blue obtained by mixing the solutions of ferrous compound and ferricyanide, are the same compound or not? This problem was solved by means of  $^{57}\text{Fe}$  Mössbauer spectroscopy in 1968 [30]. According to the  $^{57}\text{Fe}$  Mössbauer spectroscopy, Prussian blue and Turnbull’s blue are essentially the same compound, in spite of the different synthesis processes. Figure 6.13 shows the  $^{57}\text{Fe}$  Mössbauer spectra for the soluble Prussian blue, insoluble Prussian blue, and Turnbull’s blue in the ferromagnetic ordered phase ( $T_C = 5.5$  K) at 1.6 K [30]. These spectra show the superposition of a central peak corresponding to the LS state ( $S = 0$ ) of  $\text{Fe}^{\text{II}}$  coordinated by six C atoms and six magnetically split branches corresponding to the HS state ( $S = 5/2$ ) of  $\text{Fe}^{\text{III}}$  coordinated by six N atoms. The estimated internal magnetic fields of  $\text{Fe}^{\text{III}}$  ( $S = 5/2$ ) at 1.6 K were estimated at  $53.6 \pm 2$ ,  $54.1 \pm 2$  and  $54.3 \pm 2$  T for the soluble Prussian blue, insoluble Prussian blue and Turnbull’s blue, respectively.

In connection with Turnbull’s blue, the following should be noted. As shown in Fig. 6.14, in the precipitation process of Turnbull’s blue by adding  $^{57}\text{Fe}^{2+}$  to the aqueous solution of  $\text{K}_3[\text{Fe}^{\text{III}}(\text{CN})_6]$ , an electron of  $^{57}\text{Fe}^{2+}$  transfers to the  $\text{Fe}^{\text{III}}$  site in  $[\text{Fe}^{\text{III}}(\text{CN})_6]^{3-}$  and Turnbull’s blue,  $\text{KFe}^{\text{II}}\text{Fe}^{\text{III}}(\text{CN})_6$ , is precipitated [31].

In connection with Prussian blue, one of the most fascinating phenomena is the photo-induced magnetism of Prussian blue analogues by means of IVCT. In 1996, O. Sato, K. Hashimoto, et al. first reported a photo-induced ferrimagnetic phase for  $\text{K}_{0.2}\text{Co}_{1.4}[\text{Fe}(\text{CN})_6] \cdot 6.9\text{H}_2\text{O}$  [32] and  $\text{K}_{0.4}\text{Co}_{1.3}[\text{Fe}^{\text{II}}(\text{CN})_6] \cdot 5\text{H}_2\text{O}$  [33]. In the case of  $\text{K}_{0.4}\text{Co}_{0.3}^{\text{II}}\text{Co}^{\text{III}}[\text{Fe}^{\text{II}}(\text{CN})_6] \cdot 5\text{H}_2\text{O}$ , the electronic state of the Fe–CN–Co framework before light irradiation is  $\text{Fe}^{\text{II}}(t_{2g}^6 e_g^0, S = 0) - \text{CN} - \text{Co}^{\text{III}}(t_{2g}^6 e_g^0, S = 0)$  at 5 K. Visible light ( $\lambda = 500\text{--}750$  nm) irradiation at 5 K induces the IVCT, forming the excited state of  $\text{Fe}^{\text{III}}(t_{2g}^5 e_g^1, S = 1/2) - \text{CN} - \text{Co}^{\text{II}}(t_{2g}^6 e_g^0, S = 1/2)$ . Subsequently, this excited state

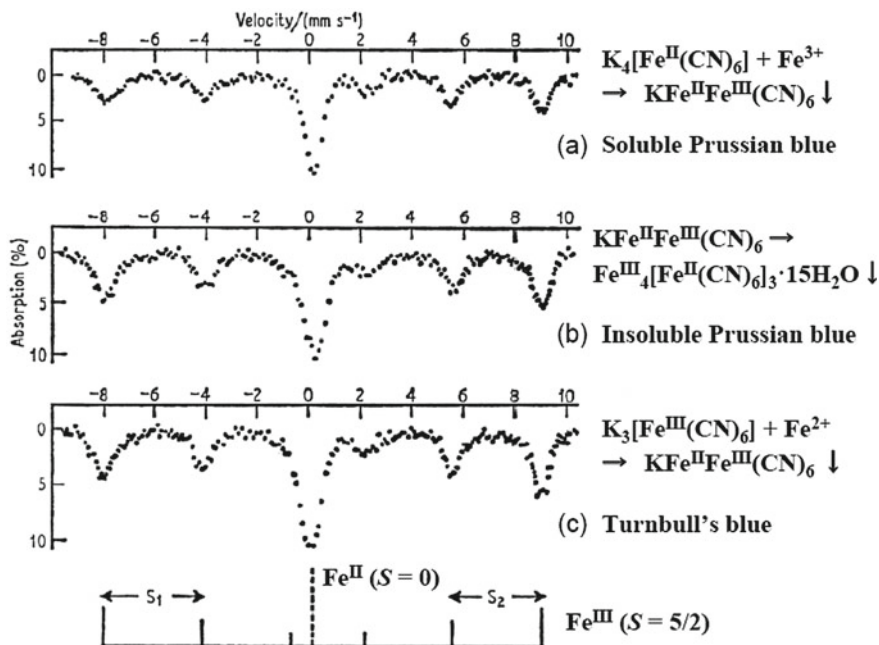


**Fig. 6.13**  $^{57}\text{Fe}$  Mössbauer spectra of **a** soluble Prussian blue, **b** insoluble Prussian blue and **c** Turnbull's blue at 1.6 K. Reprinted from [30], with the permission of AIP Publishing



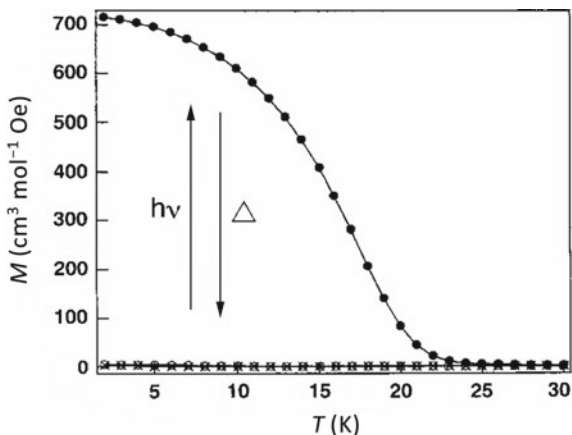
**Fig. 6.14** Formation process of Turnbull's blue

relaxes to the meta-stable state of  $\text{Fe}^{\text{III}}(t_{2g}^5 e_g^0, S = 1/2)\text{---CN---Co}^{\text{II}}(t_{2g}^5 e_g^0, S = 3/2)$ . While the compound before light irradiation is paramagnetic, that after the visible light irradiation exhibits a meta-stable ferrimagnetic phase, which can be reconverted to the initial phase by near-IR light ( $\lambda = 1319$  nm) irradiation or a thermal treatment [33]. Since then, not only Prussian blue analogues but also various CN-bridged compounds exhibiting photo-induced magnetism have been reported [34]. In addition to the photo-induced magnetism, since the discovery of thermally induced charge-transfer induced spin transition (CTIST) for  $\text{Na}_{0.4}\text{Co}_{1.3}[\text{Fe}(\text{CN})_6]\cdot 5\text{H}_2\text{O}$  in 1997 [35], several Prussian blue analogues and CN-bridged compounds exhibiting thermally induced CTIST or CTPT have been reported [36].

Figure 6.15 shows the photo-induced ferrimagnetic transition for  $\text{Rb}_{0.66}\text{Co}_{1.25}[\text{Fe}(\text{CN})_6]\cdot 4.3\text{H}_2\text{O}$  by using IVCT [37]. While  $\text{Rb}_{0.66}\text{Co}_{1.25}[\text{Fe}(\text{CN})_6]\cdot 4.3\text{H}_2\text{O}$  before the light irradiation is paramagnetic in



**Fig. 6.15** Field-cooled magnetization (FCM) curves for  $\text{Rb}_{0.66}\text{Co}_{1.25}[\text{Fe}(\text{CN})_6]\cdot 4.3\text{H}_2\text{O}$  before and after light irradiation ( $h\nu$ ) at  $H = 0.5$  T.  $\circ$ : before light irradiation,  $\bullet$ : after light irradiation,  $\times$ : after thermal treatment ( $\Delta$ ) at 150 K. Reprinted with permission from [37]. Copyright 1999 American Chemical Society



the whole temperature region, that after the light irradiation corresponding to the IVCT (500–750 nm) exhibits a meta-stable ferrimagnetic phase with  $T_N = 22$  K.

Figure 6.16 shows the  $^{57}\text{Fe}$  Mössbauer spectra before and after the light irradiation corresponding to the IVCT (500–750 nm) at 25 K [37]. Before the light irradiation, the single peak with  $IS = 0.02 \pm 0.01$  mm/s and  $QS = 0.15 \pm 0.01$  mm/s is assigned to the LS state ( $S = 0$ ) of  $\text{Fe}^{\text{II}}$ . After the light irradiation at 25 K, the single peak corresponding to the LS state of  $\text{Fe}^{\text{II}}$  was significantly reduced and a new doublet with  $IS = 0.09 \pm 0.01$  mm/s and  $QS = 1.13 \pm 0.01$  mm/s assigned to the LS state ( $S = 1/2$ ) of  $\text{Fe}^{\text{III}}$ . As a result of the light-induced CT from the  $\text{Fe}^{\text{II}}$  site to the  $\text{Co}^{\text{III}}$  site,  $\text{Rb}_{0.66}\text{Co}_{1.25}[\text{Fe}(\text{CN})_6]\cdot 4.3\text{H}_2\text{O}$  was converted from the paramagnet to the ferrimagnet with  $T_N = 22$  K, which is schematically shown in Fig. 6.17.

### 6.3.3 Mixed-Valence System, $A[\text{Fe}^{\text{II}}\text{Fe}^{\text{III}}(\text{dto})_3]$ ( $A =$ Counter Cation; $\text{dto} = \text{C}_2\text{O}_2\text{S}_2$ ), and the Charge Transfer Phase Transition

Among various kinds of multifunctional compounds, in the case of mixed-valence system whose spin states are situated in the spin crossover region, it is expected that new types of synergetic phenomena induced by both of spin and charge appear between different metal ions in order to minimize the Gibbs energy. Based on this viewpoint, we have developed a ferromagnetic organic–inorganic hybrid system,  $A[\text{Fe}^{\text{II}}\text{Fe}^{\text{III}}(\text{dto})_3]$  ( $A = (n\text{-C}_n\text{H}_{2n+1})_4\text{N}$ , spiropyran, etc.), and investigated their synergetic properties coupled with spin, charge and photon [4]. The single-crystal X-ray structural analysis of  $(n\text{-C}_3\text{H}_7)_4\text{N}[\text{Fe}^{\text{II}}\text{Fe}^{\text{III}}(\text{dto})_3]$  reveals the existence of the honeycomb network structure of  $[\text{Fe}^{\text{II}}\text{Fe}^{\text{III}}(\text{dto})_3]$ , and the  $(n\text{-C}_3\text{H}_7)_4\text{N}^+$  layer is intercalated between two adjacent  $[\text{Fe}^{\text{II}}\text{Fe}^{\text{III}}(\text{dto})_3]$  layers [20], whose structure is common for  $A[\text{M}^{\text{II}}\text{M}^{\text{III}}\text{X}_3]$  ( $A =$  cation,  $X = \text{ox}$ ,  $\text{dto}$ ,  $\text{mto}$ ).

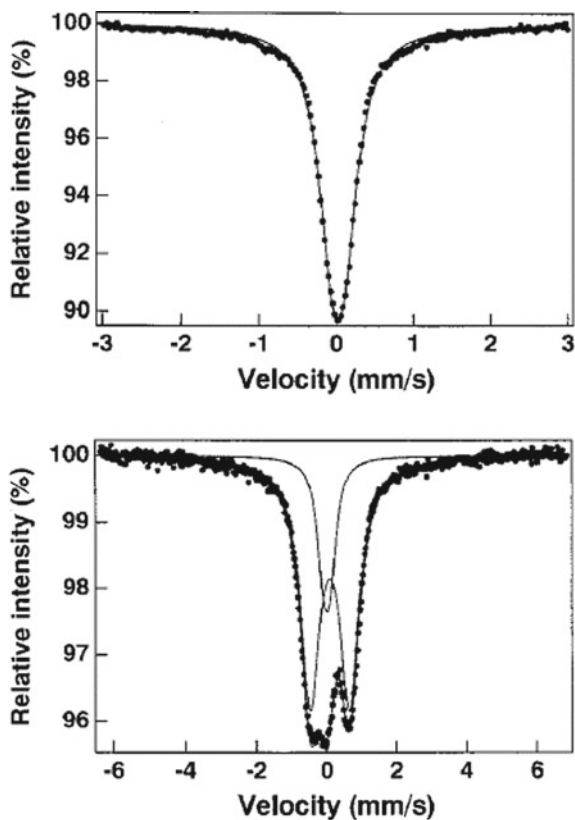


**Fig. 6.16**  $^{57}\text{Fe}$  Mössbauer spectra of  $\text{Rb}_{0.66}\text{Co}_{1.25}[\text{Fe}(\text{CN})_6]\cdot 4.3\text{H}_2\text{O}$  before and after the light irradiation of 500–750 nm at 25 K [37]

In order to investigate the electronic properties and the valence states of  $\text{Fe}^{\text{II}}$  and  $\text{Fe}^{\text{III}}$  of  $(n\text{-C}_3\text{H}_7)_4\text{N}[\text{Fe}^{\text{II}}\text{Fe}^{\text{III}}(\text{dto})_3]$  by means of  $^{57}\text{Fe}$  Mössbauer spectroscopy, we employed  $^{57}\text{Fe}$  enriched complexes,  $(n\text{-C}_3\text{H}_7)_4\text{N}[^{57}\text{Fe}^{\text{II}}\text{Fe}^{\text{III}}(\text{dto})_3]$  and  $(n\text{-C}_3\text{H}_7)_4\text{N}[\text{Fe}^{\text{II}}^{57}\text{Fe}^{\text{III}}(\text{dto})_3]$ , in which  $\text{Fe}^{\text{II}}$  or  $\text{Fe}^{\text{III}}$  was substituted with  $^{57}\text{Fe}$  (96%) [38]. In the case of  $(n\text{-C}_3\text{H}_7)_4\text{N}[^{57}\text{Fe}^{\text{II}}\text{Fe}^{\text{III}}(\text{dto})_3]$ , a solution of  $^{57}\text{FeCl}_2\cdot 4\text{H}_2\text{O}$  and  $(n\text{-C}_3\text{H}_7)_4\text{NBr}$  in a methanol/water mixture was added to a solution of  $\text{KBa}[\text{Fe}^{\text{III}}(\text{dto})_3]$ , then black powdered crystals of  $(n\text{-C}_3\text{H}_7)_4\text{N}[^{57}\text{Fe}^{\text{II}}\text{Fe}^{\text{III}}(\text{dto})_3]$  were precipitated.  $(n\text{-C}_3\text{H}_7)_4\text{N}[\text{Fe}^{\text{II}}^{57}\text{Fe}^{\text{III}}(\text{dto})_3]$  was also obtained by using  $\text{FeCl}_2\cdot 4\text{H}_2\text{O}$ ,  $(n\text{-C}_3\text{H}_7)_4\text{NBr}$  and  $\text{KBa}[^{57}\text{Fe}^{\text{III}}(\text{dto})_3]$ . Figure 6.18 shows the  $^{57}\text{Fe}$  Mössbauer spectra of  $(n\text{-C}_3\text{H}_7)_4\text{N}[^{57}\text{Fe}^{\text{II}}\text{Fe}^{\text{III}}(\text{dto})_3]$  and  $(n\text{-C}_3\text{H}_7)_4\text{N}[\text{Fe}^{\text{II}}^{57}\text{Fe}^{\text{III}}(\text{dto})_3]$  at 200 and 60 K. In the case of the  $^{57}\text{Fe}$  Mössbauer spectra of  $(n\text{-C}_3\text{H}_7)_4\text{N}[^{57}\text{Fe}^{\text{II}}\text{Fe}^{\text{III}}(\text{dto})_3]$  at 200 K, the dominant doublet (74.5% area) with  $IS = 1.18 \text{ mm s}^{-1}$  and  $QS = 1.36 \text{ mm s}^{-1}$  is assigned to the  $\text{Fe}^{\text{II}}(t_{2g}^4 e_g^2, S = 2)$  site coordinated by six O atoms. These values of  $IS$  and  $QS$  are quite similar to those ( $IS = 1.18 \text{ mm s}^{-1}$ ,  $QS = 1.26 \text{ mm s}^{-1}$ ) of the  $^{57}\text{Fe}$  Mössbauer spectrum for the  $\text{Fe}^{\text{II}}(t_{2g}^4 e_g^2, S = 2)$  site in  $(n\text{-C}_4\text{H}_9)_4\text{N}[\text{Fe}^{\text{II}}\text{Cr}^{\text{III}}(\text{ox})_3]$

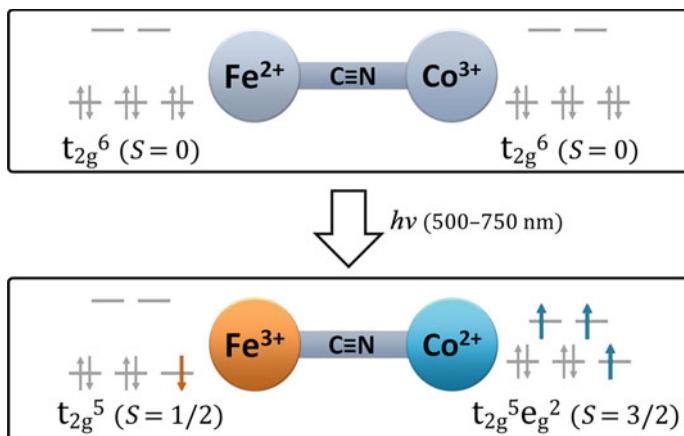


**Fig. 6.17** Schematic representation of the photo-induced magnet for  $\text{Rb}_{0.66}\text{Co}_{1.25}[\text{Fe}(\text{CN})_6]\cdot 4.3\text{H}_2\text{O}$

[39]. As shown in Fig. 6.18, the line profile of the  $^{57}\text{Fe}$  Mössbauer spectra of  $(n\text{-C}_3\text{H}_7)_4\text{N}[\text{Fe}^{\text{II}}\text{Fe}^{\text{III}}(\text{dto})_3]$  dramatically changes between 200 and 60 K. The intensity of the dominant doublet corresponding to the  $\text{Fe}^{\text{II}}$  ( $S=2$ ) site decreases and a new doublet with  $IS=0.55\text{ mm s}^{-1}$  and  $QS=0.91\text{ mm s}^{-1}$  appears. The  $IS$  and  $QS$  values of the new doublet are quite similar to those ( $IS=0.49\text{ mm s}^{-1}$ ,  $QS=0.68\text{ mm s}^{-1}$ ) of the  $^{57}\text{Fe}$  Mössbauer spectrum for the  $\text{Fe}^{\text{III}}$  ( $t_{2g}^5 e_g^2$ ,  $S=5/2$ ) site in  $(n\text{-C}_4\text{H}_9)_4\text{N}[\text{Ni}^{\text{II}}\text{Fe}^{\text{III}}(\text{ox})_3]$  at 78 K [40]. On the other hand, in the case of  $(n\text{-C}_3\text{H}_7)_4\text{N}[\text{Fe}^{\text{II}}\text{Fe}^{\text{III}}(\text{dto})_3]$  at 200 K, the dominant doublet with  $IS=0.33\text{ mm s}^{-1}$  and  $QS=0.36\text{ mm s}^{-1}$  is assigned to the  $\text{Fe}^{\text{III}}$  ( $t_{2g}^5$ ,  $S=1/2$ ) site coordinated by six S atoms. These values of  $IS$  and  $QS$  are quite similar to those ( $IS=0.33\text{ mm s}^{-1}$ ,  $QS=0.35\text{ mm s}^{-1}$  at 196 K) for the  $\text{Fe}^{\text{III}}$  ( $t_{2g}^5$ ,  $S=1/2$ ) site coordinated by six S atoms in  $\text{KBa}[\text{Fe}^{\text{III}}(\text{dto})_3]$  [41]. On the other hand, the dominant doublet with  $IS=0.41\text{ mm s}^{-1}$  and  $QS=0.51\text{ mm s}^{-1}$  at 60 K is assigned to the  $\text{Fe}^{\text{II}}$  ( $t_{2g}^6$ ,  $S=0$ ) site coordinated by six S atoms. These  $IS$  and  $QS$  values are quite similar to those ( $IS=0.41\text{ mm s}^{-1}$ ,  $QS=0.64\text{ mm s}^{-1}$  at 77 K) for the  $\text{Fe}^{\text{II}}$  ( $t_{2g}^6$ ,  $S=0$ ) site coordinated by six S atoms in pyrite ( $\text{FeS}_2$ ) [42]. In this manner, we have elucidated the CTPT for  $(n\text{-C}_3\text{H}_7)_4\text{N}[\text{Fe}^{\text{II}}\text{Fe}^{\text{III}}(\text{dto})_3]$  by means of  $^{57}\text{Fe}$  Mössbauer spectroscopy.

As mentioned above,  $(n\text{-C}_3\text{H}_7)_4\text{N}[\text{Fe}^{\text{II}}\text{Fe}^{\text{III}}(\text{dto})_3]$  undergoes the CTPT between 200 and 60 K. In order to determine the critical temperature ( $T_{\text{CT}}$ ) of CTPT,  $^{57}\text{Fe}$  Mössbauer spectroscopy was carried out in the temperature range between 130 and 90 K. As shown in Fig. 6.19, the HT phase with  $\text{Fe}^{\text{II}}\text{O}_6$  ( $S=2$ )– $\text{Fe}^{\text{III}}\text{S}_6$  ( $S=1/2$ ) and the LT phase with  $\text{Fe}^{\text{II}}\text{S}_6$  ( $S=0$ )– $\text{Fe}^{\text{III}}\text{O}_6$  ( $S=5/2$ ) are clearly distinguished in the vicinity of CTPT, which implies that the frequency of electron transfer between the  $\text{Fe}^{\text{II}}$  and  $\text{Fe}^{\text{III}}$  sites at the CTPT is at least slower than the time scale ( $10^{-7}\text{ s}$ ) of  $^{57}\text{Fe}$  Mössbauer spectroscopy. When the temperature decreases from 130 to 90 K, the fractions of HT and LT phases decrease and increase, respectively. The crossing

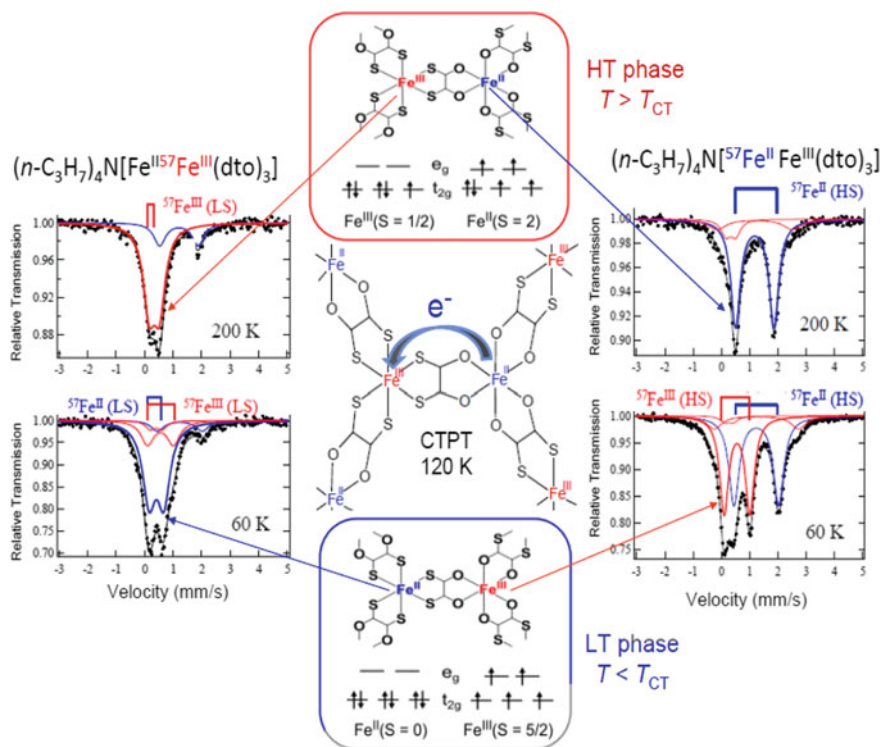


**Fig. 6.18**  $^{57}\text{Fe}$  Mössbauer spectra below and above the CTPT ( $T_{\text{CT}} \approx 120$  K) for  $(n\text{-C}_3\text{H}_7)_4\text{N}[\text{Fe}^{\text{II}}\text{Fe}^{\text{III}}(\text{dto})_3]$  and  $(n\text{-C}_3\text{H}_7)_4\text{N}[\text{Fe}^{\text{II}}\text{Fe}^{\text{III}}(\text{dto})_3]$ , and the schematic representation of CTPT. The HT phase ( $T > T_{\text{CT}}$ ) and LT phase ( $T < T_{\text{CT}}$ ) indicate the high temperature phase with  $\text{Fe}^{\text{III}}\text{S}_6(t_{2g}^5) - \text{Fe}^{\text{II}}\text{O}_6(t_{2g}^4 e_g^2)$  and the low temperature phase with  $\text{Fe}^{\text{II}}\text{S}_6(t_{2g}^6) - \text{Fe}^{\text{III}}\text{O}_6(t_{2g}^3 e_g^2)$ , respectively

point between the HT phase and LT phase components is about 122 K, which is consistent with the critical temperature (122.4 K) of CTPT determined by the heat capacity [43].

In order to confirm the direct evidence of charge transfer between the  $\text{Fe}^{\text{II}}$  and  $\text{Fe}^{\text{III}}$  sites in  $(n\text{-C}_3\text{H}_7)_4\text{N}[\text{Fe}^{\text{II}}\text{Fe}^{\text{III}}(\text{dto})_3]$ , the electrical resistivity was measured along the parallel and perpendicular directions to the  $[\text{Fe}^{\text{II}}\text{Fe}^{\text{III}}(\text{dto})_3]$  layer under several applied pressures [44]. At 0.5 GPa,  $(n\text{-C}_3\text{H}_7)_4\text{N}[\text{Fe}^{\text{II}}\text{Fe}^{\text{III}}(\text{dto})_3]$  behaves as a semiconductor as shown in Fig. 6.20. Above 0.9 GPa, on the other hand, both of the intra- and inter-layer resistivities show an anomalous drop with thermal hysteresis due to the CTPT. The intra-layer resistivity as a function of temperature at 0.9 GPa exhibits a plateau in the middle range of hysteresis loop, while an abrupt drop of resistivity appears in the inter-layer resistivity. Similar behavior appears at 1.5 GPa except for the temperature shift of the hysteresis loop. The temperature of hysteresis loop increases with increasing applied pressure, which is consistent with that of the magnetic susceptibility under applied pressures [45]. The activation energies at 0,

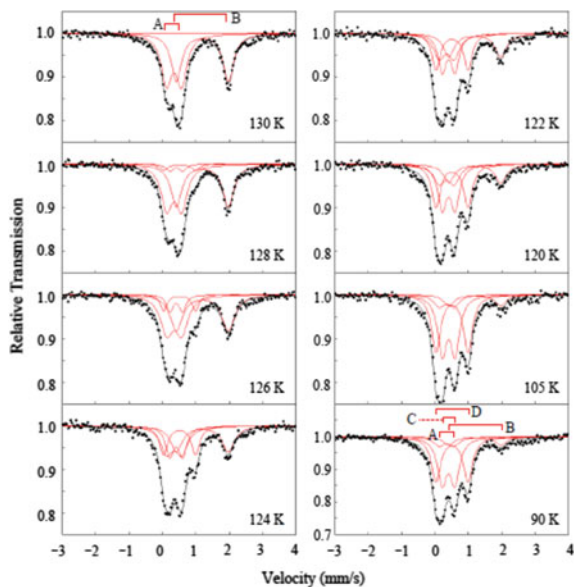


**Fig. 6.19**  $^{57}\text{Fe}$  Mössbauer spectra of  $(n\text{-C}_3\text{H}_7)_4\text{N}[\text{Fe}^{\text{II}}\text{Fe}^{\text{III}}(\text{dto})_3]$  in the vicinity of CTPT ( $T_{\text{CT}} = 122$  K). A:  $\text{Fe}^{\text{III}}$  ( $S = 1/2$ ), B:  $\text{Fe}^{\text{II}}$  ( $S = 2$ ), C:  $\text{Fe}^{\text{II}}$  ( $S = 0$ ), D:  $\text{Fe}^{\text{III}}$  ( $S = 5/2$ )

0.9 and 1.5 GPa are 1700, 1400 and 1200 K, respectively. The anomalous drop in the resistivity as a function of temperature is attributed to the electron transfer between the  $t_{2g}$  orbitals of the  $\text{Fe}^{\text{II}}$  and  $\text{Fe}^{\text{III}}$  sites in the temperature region of CTPT.

### 6.3.4 Dynamics of Charge Transfer Phase Transition in $A[\text{Fe}^{\text{II}}\text{Fe}^{\text{III}}(\text{dto})_3]$ by Means of Muon Spectroscopy

Muon spin relaxation ( $\mu\text{SR}$ ) is one of the most powerful methods to investigate the magnitude, distribution or fluctuation of internal magnetic field. Therefore, the  $\mu\text{SR}$  technique has been applied to the study of magnetic phase transitions, various kinds of spin frustrations, superconducting phenomena and so forth [46]. The asymmetry parameter of  $\mu\text{SR}$  is defined as  $A(t) = [N_{\text{B}}(t) - N_{\text{F}}(t)]/[N_{\text{B}}(t) + N_{\text{F}}(t)]$ , in which  $N_{\text{F}}(t)$  and  $N_{\text{B}}(t)$  are the total muon events of the forward and backward counters in the muon beam line, respectively. The initial asymmetry,  $A(0)$ , is defined as the asymmetry at  $t = 0$ . In order to analyze the time spectra of  $A(t)$ , the following function with two components was used [46],

$$A_0 G_Z(\Delta, H_{\text{LF}}, t) \exp(-\lambda_0 t) + A_1 \exp(-\lambda_1 t) \quad (6.4)$$

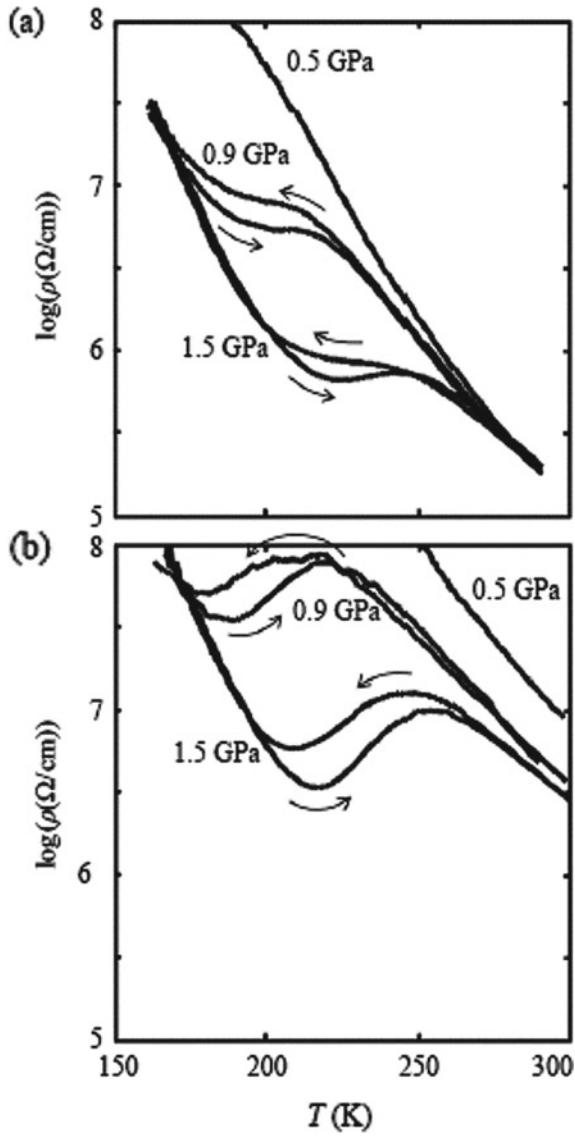


**Fig. 6.20** Temperature dependence of **a** intra-layer and **b** inter-layer electrical resistivities of  $(n\text{-C}_3\text{H}_7)_4\text{N}[\text{Fe}^{\text{II}}\text{Fe}^{\text{III}}(\text{dto})_3]$  under several applied pressures. Arrows denote the direction of heating or cooling process. Reprinted from [44], Copyright 2003, with permission from Elsevier

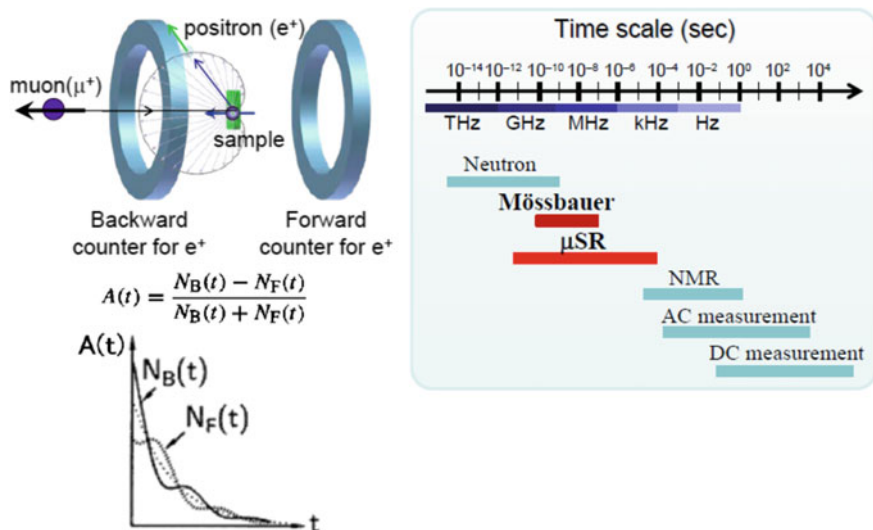


Fig. 6.21 Schematic representation of muon spectroscopy and its time scale

where  $A_0$  and  $A_1$  are the initial asymmetries of the slow and fast relaxation components,  $\lambda_0$  and  $\lambda_1$  are the respective muon spin depolarization rates.  $G_Z(\Delta, H_{LF}, t)$  is the static Kubo–Toyabe function [47].  $\Delta/\gamma_\mu$  is the distribution width of the nuclear-dipole fields at the muon sites, and  $\gamma_\mu$  is the gyromagnetic ratio of muon spin.  $H_{LF}$  is the longitudinal magnetic field. Figure 6.21 shows the time scale and the schematic representation of muon spectroscopy.

Figure 6.22 shows the time dependence of the asymmetry parameter,  $A(t) = [N_B(t) - N_F(t)]/[N_B(t) + N_F(t)]$  of  $\mu$ SR for  $(n\text{-C}_3\text{H}_7)_4\text{N}[\text{Fe}^{\text{II}}\text{Fe}^{\text{III}}(\text{dto})_3]$  at various temperatures under zero-field [5]. From the analysis of time spectra of  $\mu$ SR by using Eq. (6.4), we obtained the depolarization rate ( $\lambda_0$ ) as a function of temperature for  $(n\text{-C}_n\text{H}_{2n+1})_4\text{N}[\text{Fe}^{\text{II}}\text{Fe}^{\text{III}}(\text{dto})_3]$ .

Figure 6.23 shows the depolarization rate ( $\lambda_0$ ) of muon spin as a function of temperature under various longitudinal magnetic fields for  $(n\text{-C}_n\text{H}_{2n+1})_4\text{N}[\text{Fe}^{\text{II}}\text{Fe}^{\text{III}}(\text{dto})_3]$  ( $n = 3, 5$ ). In the case of  $n = 3$ , an anomalous enhancement of depolarization rate appears at around 80 K. This anomalous peak decreases with increasing the longitudinal field, and eventually disappears at about 10 mT (= 100 Oe). In the case of  $n = 5$ , on the other hand, any anomalous peak does not appear between 200 and 40 K. Therefore, the anomalous enhancement of depolarization rate at around 80 K for  $n = 3$  is attributed to the frequency of electron transfer between the  $\text{Fe}^{\text{II}}$  and  $\text{Fe}^{\text{III}}$  sites at the CTPT, which induces the fluctuating internal magnetic field at the muon site.

As shown in Fig. 6.23, the depolarization rates for  $n = 3$  and  $n = 5$  decrease with increasing longitudinal field up to 10 mT and become almost constant above 10 mT. The constant value increases with decreasing temperature from 200 to 40 K, which

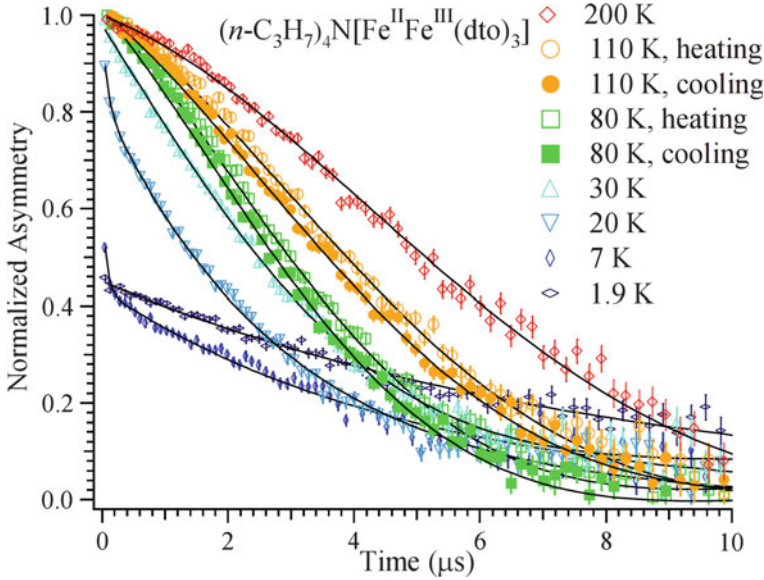


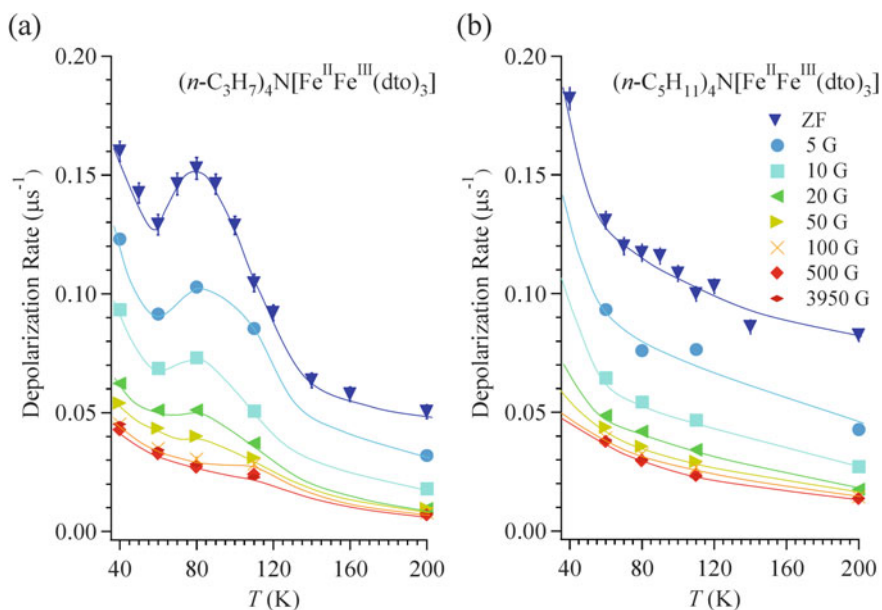
**Fig. 6.22** Time dependence of the asymmetry parameter,  $A(t) = [N_B(t) - N_F(t)]/[N_B(t) + N_F(t)]$  of  $\mu$ SR for  $(n\text{-C}_3\text{H}_7)_4\text{N}[\text{Fe}^{\text{II}}\text{Fe}^{\text{III}}(\text{dto})_3]$  at several temperatures under zero-field [5]. Reprinted figure with permission from [5]. Copyright 2008 by the American Physical Society

suggests the existence of two components. One component is easily suppressed by 10 mT, while the other component remains even at 400 mT ( $= 4000$  Oe). The former component implies that there is a weak and slowly fluctuating internal magnetic field at the muon site, which is easily masked by 10 mT, which is attributed to the fluctuating component of nuclear dipoles such as MnSi [48]. On the other hand, considering that the latter component increases with decreasing temperature and similar values of the depolarization rate are observed for  $n = 3$  and 5 in the same temperature region, which implies that the latter component is attributed to the dipole field due to the fluctuation of paramagnetic Fe spins.

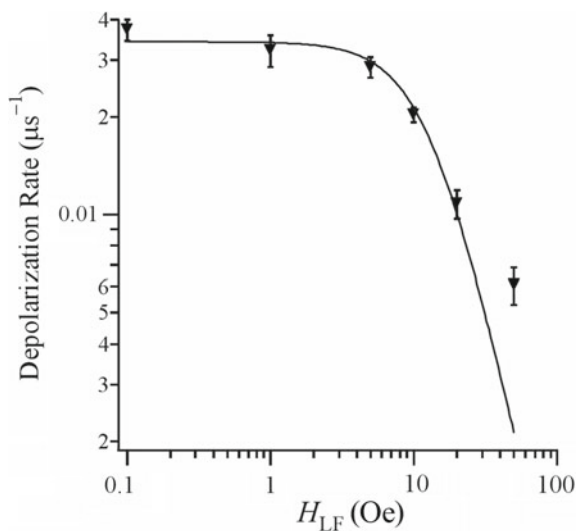
As for the anomalous enhancement of the depolarization rate of muon spin induced by the CTPT, we extract the difference of depolarization rate between those of  $n = 3$  and 5 to analyze the frequency of electron transfer between the  $\text{Fe}^{\text{II}}$  and  $\text{Fe}^{\text{III}}$  sites at the CTPT. The longitudinal field dependence of this subtracted depolarization rate at 80 K is plotted in Fig. 6.24. By using the Redfield equation [49] for the longitudinal field ( $H_{\text{LF}}$ ) dependence of the subtracted depolarization rate ( $\lambda_{\text{CT}}$ ) between  $n = 3$  and 5, we determined the correlation time of muon spins ( $\tau_c$ ) and the amplitude of fluctuating internal magnetic field ( $H_{\text{loc}}$ ) at the muon site, respectively. The Redfield equation is expressed as follows,

$$\lambda_{\text{CT}} = \frac{2\gamma_{\mu}^2 H_{\text{loc}}^2 \tau_c}{1 + \gamma_{\mu}^2 H_{\text{LF}}^2 \tau_c^2} \quad (6.5)$$





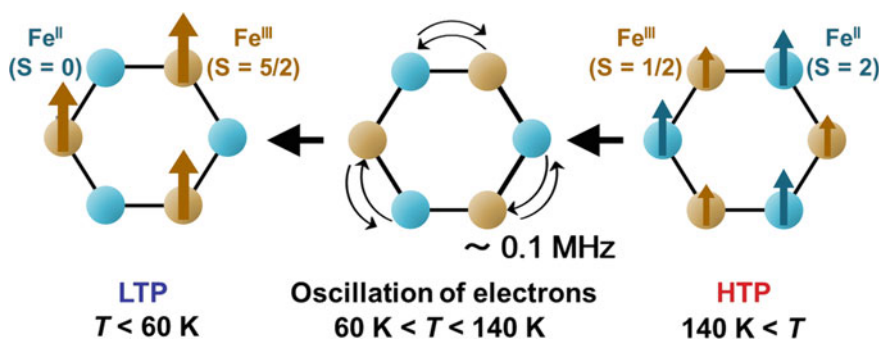
**Fig. 6.23** Temperature and longitudinal-field dependence of the muon spin depolarization rate,  $\lambda_0$ , for  $(n\text{-C}_3\text{H}_7)_4\text{N}[\text{Fe}^{\text{II}}\text{Fe}^{\text{III}}(\text{dto})_3]$  and  $(n\text{-C}_5\text{H}_{11})_4\text{N}[\text{Fe}^{\text{II}}\text{Fe}^{\text{III}}(\text{dto})_3]$ . 1 Oe = 0.1 mT. The solid lines are guides for eye. Reprinted figure with permission from [5]. Copyright 2008 by the American Physical Society



**Fig. 6.24** Subtracted depolarization rate ( $\lambda_{CT}$ ) between  $n = 3$  and  $5$  as a function of applied longitudinal magnetic field for  $(n\text{-C}_n\text{H}_{2n+1})_4\text{N}[\text{Fe}^{\text{II}}\text{Fe}^{\text{III}}(\text{dto})_3]$  at 80 K in the cooling process. The solid line shows the best fit of the Redfield equation. 1 Oe = 0.1 mT. Reprinted figure with permission from [5]. Copyright 2008 by the American Physical Society

**Table 6.1** Parameters obtained by fitting the Redfield equation to the subtracted depolarization rate ( $\lambda_{CT}$ ) between  $n = 3$  and 5 for  $(n\text{-C}_n\text{H}_{2n+1})_4\text{N}[\text{Fe}^{\text{II}}\text{Fe}^{\text{III}}(\text{dto})_3]$  [5]

$T$ (K)	$\tau_c$ ( $\mu\text{s}$ )	$H_{\text{loc}}$ (mT)
60	–	0
80	5.7	0.40
110	10.6	0.19

**Fig. 6.25** Schematic representation of the valence fluctuation between the  $\text{Fe}^{\text{II}}$  and  $\text{Fe}^{\text{III}}$  sites at the CTPT for  $(n\text{-C}_3\text{H}_7)_4\text{N}[\text{Fe}^{\text{II}}\text{Fe}^{\text{III}}(\text{dto})_3]$ 

where  $\gamma_\mu$  is the gyromagnetic ratio of muon spin. These parameters at several temperatures are summarized in Table 6.1 [5].

The frequency of the additional internal field at the muon site induced by the CTPT, which is given as  $\nu = 1/\tau_c$ , is the order of 0.1 MHz as the maximum value at 80 K and zero at 60 K [5]. The magnitude of  $H_{\text{loc}}$  is between 0.19 and 0.40 mT, which is larger than that of nuclear dipole field ( $\sim 0.1$  mT). These results imply the fluctuation of electron transfer between the  $\text{Fe}^{\text{II}}$  and  $\text{Fe}^{\text{III}}$  sites at the CTPT, which is schematically shown in Fig. 6.25. The time scale of  $\tau_c$  is consistent with the result of the  $^{57}\text{Fe}$  Mössbauer measurement. The fluctuation of electron transfer between the  $\text{Fe}^{\text{II}}$  and  $\text{Fe}^{\text{III}}$  sites induced by the CTPT for  $(n\text{-C}_3\text{H}_7)_4\text{N}[\text{Fe}^{\text{II}}\text{Fe}^{\text{III}}(\text{dto})_3]$  is responsible for the anomalous drop with thermal hysteresis in the electrical resistivity at the CTPT.

### 6.3.5 Size Effect of Intercalated Cation on the Charge Transfer Phase Transition and Ferromagnetism for $A[\text{Fe}^{\text{II}}\text{Fe}^{\text{III}}(\text{dto})_3]$

Figure 6.26 shows the  $^{57}\text{Fe}$  Mössbauer spectra at 200, 77 and 4 K for  $(n\text{-C}_n\text{H}_{2n+1})_4\text{N}[\text{Fe}^{\text{II}}\text{Fe}^{\text{III}}(\text{dto})_3]$  ( $n = 3\text{--}6$ ) [50]. At 200 K, the line profiles of all the complexes are quite similar to each other, where two quadrupole doublets (A and

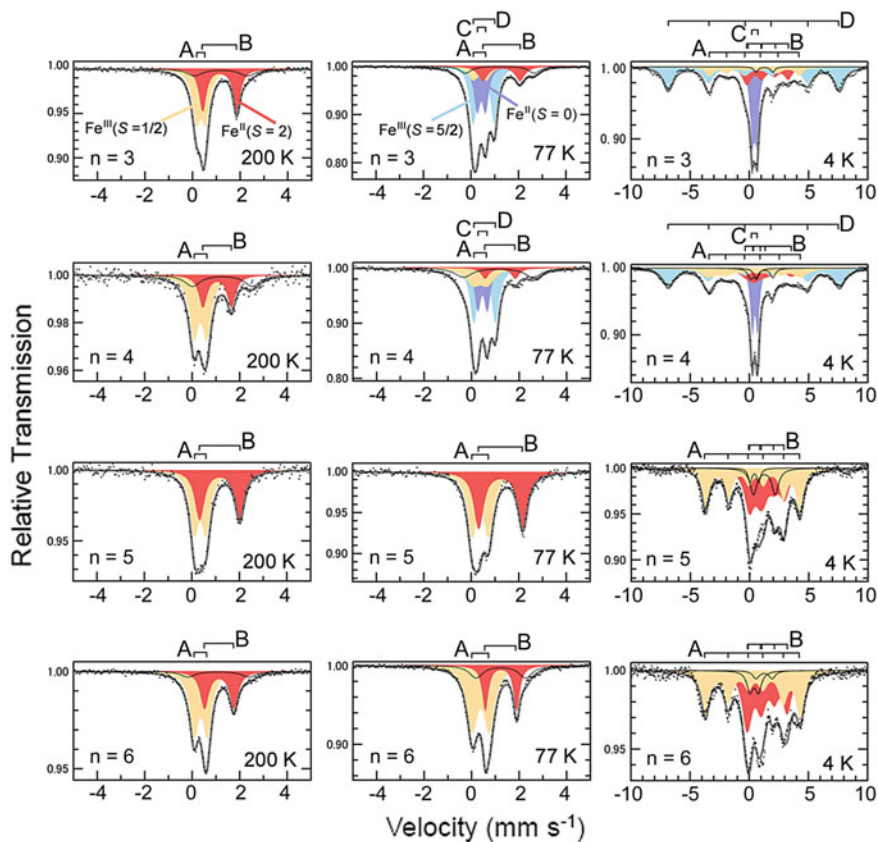


**Fig. 6.26**  $^{57}\text{Fe}$  Mössbauer spectra of  $(n\text{-C}_n\text{H}_{2n+1})_4\text{N}[\text{Fe}^{\text{II}}\text{Fe}^{\text{III}}(\text{dto})_3]$  ( $n = 3\text{--}6$ ) at 200 K, 77 K and 4 K. A:  $\text{Fe}^{\text{III}}$  ( $S = 1/2$ ), B:  $\text{Fe}^{\text{II}}$  ( $S = 2$ ), C:  $\text{Fe}^{\text{II}}$  ( $S = 0$ ), D:  $\text{Fe}^{\text{III}}$  ( $S = 5/2$ ) [50]. Reprinted with permission from [50]. Copyright 2012 Mössbauer Effect Data Center

B) mainly exist. The wider doublet (B) is assigned to the  $\text{Fe}^{\text{II}}$  ( $S = 2$ ) site coordinated by six O atoms. The  $IS$  and  $QS$  of (B) fall in the range of  $1.05\text{--}1.17\text{ mm s}^{-1}$  and  $1.20\text{--}1.69\text{ mm s}^{-1}$ , respectively. On the other hand, the narrower doublet (A) with  $IS = 0.29\text{--}0.35\text{ mm s}^{-1}$  and  $QS = 0.38\text{--}0.56\text{ mm s}^{-1}$  is assigned to the  $\text{Fe}^{\text{III}}$  ( $S = 1/2$ ) site coordinated by six S atoms.

In the cases of  $n = 3$  and 4, with decreasing temperature from 200 to 77 K, the  $^{57}\text{Fe}$  Mössbauer spectra corresponding to the HTP decrease by about 80%. Instead of these spectra, two doublets (C and D) appear. The doublet (C) with  $IS = 0.43\text{--}0.46\text{ mm s}^{-1}$  and  $QS = 0.35\text{--}0.41\text{ mm s}^{-1}$  is assigned to the  $\text{Fe}^{\text{II}}$  ( $S = 0$ ) site coordinated by six S atoms. On the other hand, the doublet (D) with  $IS = 0.54\text{--}0.55\text{ mm s}^{-1}$  and  $QS = 0.89\text{--}0.92\text{ mm s}^{-1}$  is assigned to the  $\text{Fe}^{\text{III}}$  ( $S = 5/2$ ) site coordinated by six O atoms. At 4 K, a central strong doublet (C) with  $IS = 0.43\text{--}0.45\text{ mm s}^{-1}$  and  $QS = 0.39\text{--}0.46\text{ mm s}^{-1}$ , and a sextet (D) divided from  $-8$  to  $+8\text{ mm s}^{-1}$  with a large

hyperfine field of  $H_{\text{int}} = \sim 45.0$  T are observed in the spectra of  $n = 3$  and 4. The former can be assigned to the diamagnetic state of  $\text{Fe}^{\text{II}}$  ( $S = 0$ ) and the latter is typical of the magnetically ordered state of  $\text{Fe}^{\text{III}}$  ( $S = 5/2$ ). From the analysis of  $^{57}\text{Fe}$  Mössbauer spectra for  $(n\text{-C}_n\text{H}_{2n+1})_4\text{N}[\text{Fe}^{\text{II}}\text{Fe}^{\text{III}}(\text{dto})_3]$ , it is obvious that the charge transfer between the  $\text{Fe}^{\text{II}}$  and  $\text{Fe}^{\text{III}}$  sites takes place between 200 and 77 K for  $n = 3$  and 4. At 4 K, in addition to the  $^{57}\text{Fe}$  Mössbauer spectra corresponding to the  $\text{Fe}^{\text{II}}$  ( $S = 0$ ) and  $\text{Fe}^{\text{III}}$  ( $S = 5/2$ ) sites, the sextets of the  $\text{Fe}^{\text{II}}$  ( $S = 2$ ) and  $\text{Fe}^{\text{III}}$  ( $S = 1/2$ ) sites corresponding to the HTP are also required as the relative area of *ca.* 15% (for  $n = 3$ ) or 30% (for  $n = 4$ ). In the case of  $n = 4$ , two ferromagnetic phases with  $T_C = 7$  and 13 K are clearly observed in the magnetization measurement, being consistent with the large area of the HTP at 4 K in the  $^{57}\text{Fe}$  Mössbauer spectra.

The  $^{57}\text{Fe}$  Mössbauer spectra in the ferromagnetic phases for  $n = 5$  and 6 are completely different from those for  $n = 3$  and 4. In the cases of  $n = 5$  and 6, the CTPT does not take place, so that the spectra of  $n = 5$  and 6 at 4 K can be assigned to the  $\text{Fe}^{\text{II}}$  ( $S = 2$ ) and  $\text{Fe}^{\text{III}}$  ( $S = 1/2$ ) sites in the magnetically ordered phase. The sextets of the  $\text{Fe}^{\text{III}}$  ( $S = 1/2$ ) sites have relatively large  $H_{\text{int}}$  of 24.6 T (for  $n = 5$ ) and 24.8 T (for  $n = 6$ ) at 4 K, while the  $\text{Fe}^{\text{II}}$  ( $S = 2$ ) sites have relatively small  $H_{\text{int}}$  of 7.3 T (for  $n = 5$ ) and 9.9 T (for  $n = 6$ ).

Figure 6.27 shows the  $^{57}\text{Fe}$  Mössbauer spectra for  $(n\text{-C}_n\text{H}_{2n+1})_4\text{N}[\text{Fe}^{\text{II}}\text{Fe}^{\text{III}}(\text{dto})_3]$  ( $n = 3$  and 5) in the magnetically ordered phase. In the case of  $n = 3$ , the LTP with  $\text{Fe}^{\text{II}}\text{S}_6$  ( $S = 0$ )– $\text{Fe}^{\text{III}}\text{O}_6$  ( $S = 5/2$ ) undergoes the ferromagnetic transition with  $T_C = 7.1$  K. In the case of  $n = 5$ , on the other hand, the HTP with  $\text{Fe}^{\text{II}}\text{O}_6$  ( $S = 2$ )– $\text{Fe}^{\text{III}}\text{S}_6$  ( $S = 1/2$ ) undergoes the ferromagnetic transition with  $T_C = 19.5$  K. As shown in Fig. 6.13, the  $^{57}\text{Fe}$  Mössbauer spectrum of the ferromagnetically ordered state in

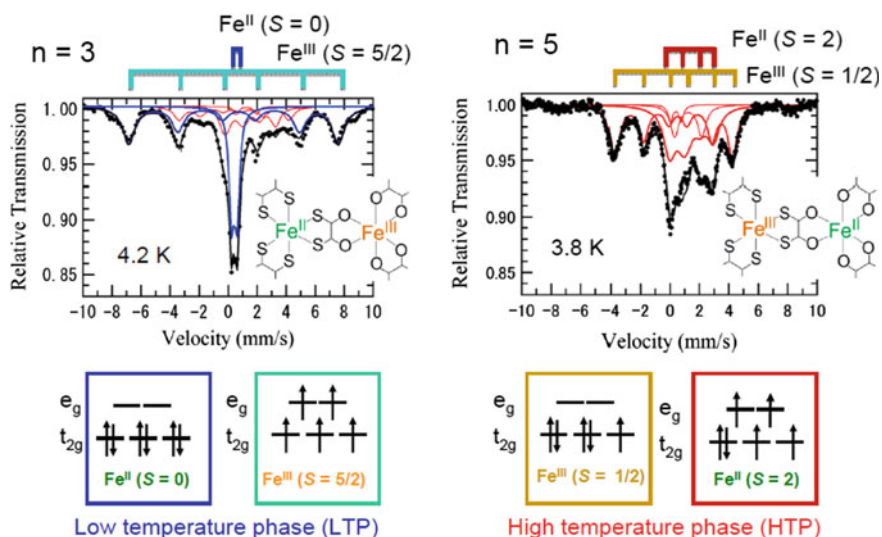


**Fig. 6.27**  $^{57}\text{Fe}$  Mössbauer spectra of  $(n\text{-C}_n\text{H}_{2n+1})_4\text{N}[\text{Fe}^{\text{II}}\text{Fe}^{\text{III}}(\text{dto})_3]$  ( $n = 3$  and 5) in the magnetically ordered phase

Prussian blue is a very informative guide to the assignment of the  $^{57}\text{Fe}$  Mössbauer spectra in magnetically ordered state for  $n = 3$  and 4. In the case of Prussian blue, the spin state of the  $\text{Fe}^{\text{II}}$  site coordinated by six C atoms of cyanide ligands is the LS state ( $t_{2g}^6$ ,  $S = 0$ ), and that of the  $\text{Fe}^{\text{III}}$  site coordinated by six N atoms is the HS state ( $t_{2g}^3 e_g^2$ ,  $S = 0$ ). The estimated  $H_{\text{int}}$  for  $\text{Fe}^{\text{II}}$  ( $t_{2g}^6$ ,  $S = 0$ ) and  $\text{Fe}^{\text{III}}$  ( $t_{2g}^3 e_g^2$ ,  $S = 5/2$ ) in  $\text{Fe}_4^{\text{III}}[\text{Fe}^{\text{II}}(\text{CN})_6]_3$  at 1.6 K are 0 and 54.0 T, respectively [30].  $^{57}\text{Fe}$  Mössbauer paramers of  $(n\text{-C}_n\text{H}_{2n+1})_4\text{N}[\text{Fe}^{\text{II}}\text{Fe}^{\text{III}}(\text{dto})_3]$  ( $n = 3\text{--}6$ ) are listed in Table 6.2.

In order to confirm the ferromagnetic phase transition, we investigated the magnetization as a function of temperature for  $n = 3\text{--}6$ , which is shown in Fig. 6.28. The Curie temperature were estimated at 7, (7 and 13), 19.5 and 23 K for  $n = 3, 4, 5,$  and

**Table 6.2**  $^{57}\text{Fe}$  Mössbauer parameters of  $(n\text{-C}_n\text{H}_{2n+1})_4\text{N}[\text{Fe}^{\text{II}}\text{Fe}^{\text{III}}(\text{dto})_3]$  ( $n = 3\text{--}6$ )

Doublet	$T$ (K)	$IS$ ( $\text{mm s}^{-1}$ ) $n =$				$QS$ ( $\text{mm s}^{-1}$ ) $n =$				$H_{\text{int}}$ (T) $n =$			
		3	4	5	6	3	4	5	6	3	4	5	6
(A) $\text{Fe}^{\text{III}}\text{S}_6$ ( $S = 1/2$ )	200	0.35	0.29	0.35	0.31	0.38	0.55	0.51	0.56	23.4	24.1	24.6	24.8
	77	0.38	0.36	0.39	0.38	0.55	0.60	0.68	0.74				
	4	0.33	0.33	0.40	0.42	0.55	0.51	0.73	0.71				
(B) $\text{Fe}^{\text{II}}\text{O}_6$ ( $S = 2$ )	200	1.14	1.05	1.17	1.14	1.43	1.20	1.69	1.24	10.2	10.0	7.3	9.9
	77	1.28	1.20	1.24	1.23	1.57	1.27	1.84	1.31				
	4	1.26	1.26	1.24	1.26	1.41	1.41	1.84	1.37				
(C) $\text{Fe}^{\text{II}}\text{S}_6$ ( $S = 0$ )	77	0.43	0.46	–	–	0.35	0.41	–	–	0	0	..	... –
	4	0.43	0.46	–	–	0.39	0.46	–	–				
(D) $\text{Fe}^{\text{III}}\text{O}_6$ ( $S = 5/2$ )	77	0.54	0.55	–	–	0.89	0.92	–	–	44.8	44.8	–	... –
	4	0.55	0.55	–	–	0.90	0.95	–	–				

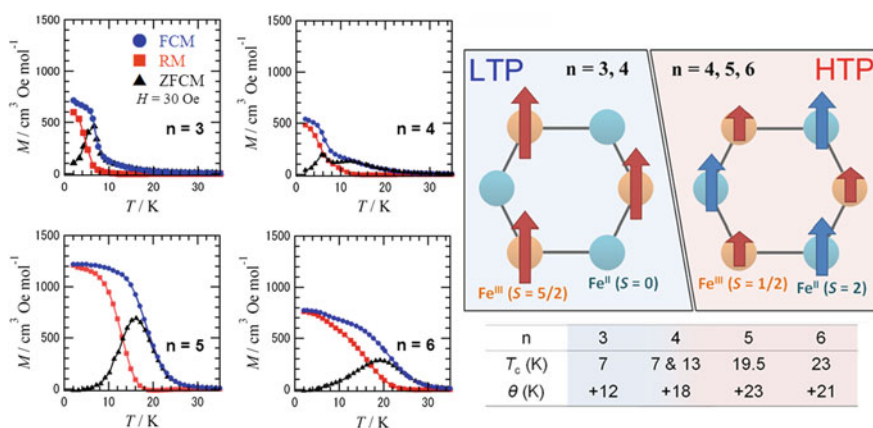


**Fig. 6.28** Magnetization of  $(n\text{-C}_n\text{H}_{2n+1})_4\text{N}[\text{Fe}^{\text{II}}\text{Fe}^{\text{III}}(\text{dto})_3]$  ( $n = 3\text{--}6$ ) as a function of temperature. FCM: field-cooled magnetization, ZFCM: zero-field-cooled magnetization, RM: remnant magnetization. FCM and ZFCM were measured at 3.0 mT. ( $= 30$  Oe).  $T_c$  and  $\theta$  denote the Curie temperature and Weiss temperature, respectively

6, respectively, from the heat capacity measurements for  $n = 3$  and 4, [2(b)] and from the analysis of Arrott plot for  $n = 5$  and 6 [6]. In the case of  $n = 4$ , the coexisting LTP and HTP undergo the ferromagnetic phase transitions at 7 K and 13 K, respectively. The critical temperature of CTPT, the Curie temperature and Weiss temperature of  $(n\text{-C}_n\text{H}_{2n+1})_4\text{N}[\text{Fe}^{\text{II}}\text{Fe}^{\text{III}}(\text{dto})_3]_{\infty}$  ( $n = 3\text{--}6$ ) are summarized in Fig. 6.28.

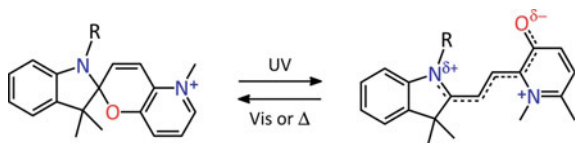
### 6.3.6 New Type of Photo-Induced Magnetism Induced by the Photo-Isomerization of Intercalated Cation

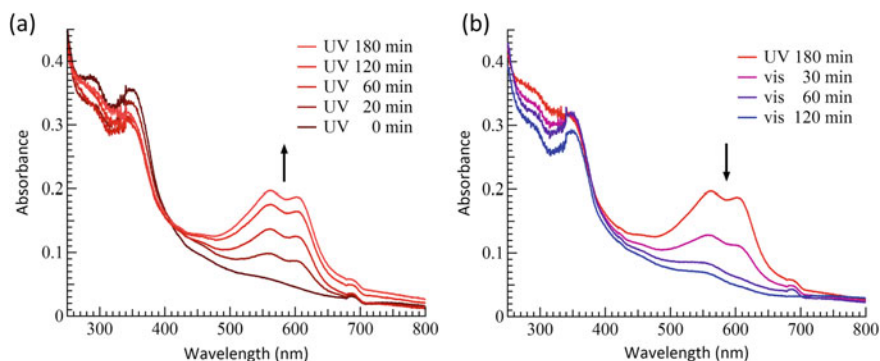
As mentioned in 6.3.4, the CTPT and the ferromagnetic phase transition of  $(n\text{-C}_n\text{H}_{2n+1})_4\text{N}[\text{Fe}^{\text{II}}\text{Fe}^{\text{III}}(\text{dto})_3]_{\infty}$  remarkably depend on the size of intercalated cation, which implies a possibility to control the CTPT and the ferromagnetic phase transition in the  $[\text{Fe}^{\text{II}}\text{Fe}^{\text{III}}(\text{dto})_3]_{\infty}^{-}$  layer by means of a photo-isomerization of intercalated cation as well as a photo-induced IVCT. In organic-inorganic hybrid systems, it is effective to use an organic photochromic molecule for producing photo-switchable materials. On the basis of this strategy, we have synthesized  $(\text{SP-R})[\text{Fe}^{\text{II}}\text{Fe}^{\text{III}}(\text{dto})_3]$  (SP-R = cationic spiropyran, R = alkyl group) [7]. In general, the cationic spiropyran can be converted from the yellow-colored closed form (CF) to the red-colored open form (OF) under UV light irradiation (330–370 nm). The OF is usually less stable and returns to the CF thermally or photo-chemically (500–600 nm). This photo-isomerization is associated with a volume change of molecule, which is schematically shown in Fig. 6.29.

Figure 6.30 shows the change of absorption spectra for  $(\text{SP-Me})[\text{Fe}^{\text{II}}\text{Fe}^{\text{III}}(\text{dto})_3]$  in a KBr pellet under UV light irradiation (350 nm with  $40 \text{ mW cm}^{-2}$ ) at 70 K [7]. At 70 K, the absorption band between 550 and 600 nm corresponding to the  $\pi\text{-}\pi^*$  transition of the OF is continuously enhanced with the increase of UV light irradiation time, meanwhile the initial black pellet changes to a deep purple pellet. After the UV light irradiation for 3 h, its intensity is almost saturated. The UV light induced OF in  $(\text{SP-Me})[\text{Fe}^{\text{II}}\text{Fe}^{\text{III}}(\text{dto})_3]$  is stable even at room temperature on dark condition. This absorption band almost disappears under visible light irradiation (white light,  $600 \text{ mW cm}^{-2}$ ) for 2 h. The photo-isomerization of cationic SP-Me from the CF to the OF by UV light irradiation and that from the OF to the CF by visible light irradiation reversibly occurs at 300 K as well as at 70 K [7].

Figure 6.31 shows the temperature dependence of the magnetization for  $(\text{SP-Me})[\text{Fe}^{\text{II}}\text{Fe}^{\text{III}}(\text{dto})_3]$  before and after the UV light irradiation at 300 and 77 K. As shown in Fig. 6.31, on the heating process, the FCM and RM curves decrease stepwise

**Fig. 6.29** Photochromic reaction of cationic spiropyran (SP-R)





**Fig. 6.30** Optical absorption of  $(\text{SP-Me})[\text{Fe}^{\text{II}}\text{Fe}^{\text{III}}(\text{dto})_3]$  in a KBr pellet under **a** UV light irradiation and **b** visible-light irradiation at 70 K. UV light irradiation (350 nm with  $40 \text{ mW cm}^{-2}$ ) on the KBr pellet was performed at first. After the saturation of light-induced absorption spectra at around 550–600 nm, visible-light irradiation (white light with  $600 \text{ mW cm}^{-2}$ ) on the pellet was performed. Reprinted with permission from [7(a)]. Copyright 2009 American Chemical Society

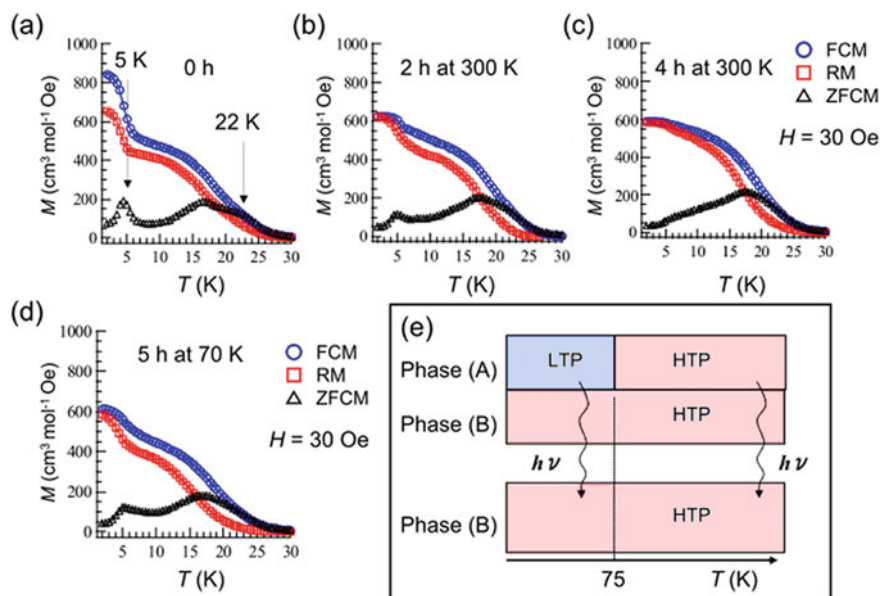


**Fig. 6.31** **a–c** Temperature dependence of the magnetization for  $(\text{SP-Me})[\text{Fe}^{\text{II}}\text{Fe}^{\text{III}}(\text{dto})_3]$  before and after the UV light irradiation (350 nm with  $40 \text{ mW cm}^{-2}$ ) for 2 and 4 h at 300 K. **d** Temperature dependence of the magnetization after the UV light irradiation for 5 h at 70 K. **e** Schematic representation of the photo-induced phase conversion from the phase (A) to the phase (B).  $T = 75 \text{ K}$  denotes the CTPT. Reprinted with permission from [7(a)]. Copyright 2009 American Chemical Society

at about 7 K and disappears at about 25 K. On the other hand, the ZFCM curve has two maxima (5 K and 17 K) and a hump at 22 K. The LTP and HTP of (SP-Me)[Fe<sup>II</sup>Fe<sup>III</sup>(dto)<sub>3</sub>] individually undergo the ferromagnetic phase transitions at 5 K and 22 K, respectively.

When the UV light (350 nm with 40 mW cm<sup>-2</sup>) is irradiated for 4 h at 300 K, the FCM and RM curves change from the stepwise magnetization curves to normal magnetization curves, and the peak of ZFCM at around 5 K disappears, being reflected by the disappearance of LTP. On the other hand, being reflected by the growth of HTP, the FCM and RM values between 5 and 22 K slightly increase after the UV light irradiation. These photo-induced effects can be explained as follows. The photo-isomerization of cationic SP-Me from CF to OF by UV irradiation leads to the expansion of its own volume, which expands the unit cell volume and destabilizes the LTP. The photo-induced phase conversion of (SP-Me)[Fe<sup>II</sup>Fe<sup>III</sup>(dto)<sub>3</sub>] is schematically shown in Fig. 6.31e, where we name two phases, (A) and (B). Only in the phase (A), the CTPT takes place. Suppose that the UV light irradiation induces the transformation from the phase (A) to the phase (B), the LTP in the phase (A) is forced to convert into the HTP in the phase (B) by UV light irradiation below 95 K. In order to confirm the CTPT in [Fe<sup>II</sup>Fe<sup>III</sup>(dto)<sub>3</sub>] induced by the photo-isomerization of spiropyran, we performed UV light irradiation at 70 K, which corresponds to the arrow of the left side in Fig. 6.31e. The FCM, RM, and ZFCM curves after UV light irradiation for 5 h at 70 K are shown in Fig. 6.31d. Indeed, the photo-induced change in the ferromagnetic property shows the same tendency as in the case of UV light irradiation for 2 h at 300 K. Therefore, It is concluded that the destabilization of LTP and the stabilization of HTP by the photo-isomerization of intercalated SP-Me<sup>+</sup> below 70 K induces the CTPT in the [Fe<sup>II</sup>Fe<sup>III</sup>(dto)<sub>3</sub>] layer.

Moreover, in order to prove the disappearance of LTP by UV light irradiation, we measured the <sup>57</sup>Fe Mössbauer spectra of (SP-Me)[Fe<sup>II</sup>Fe<sup>III</sup>(dto)<sub>3</sub>] at 6 K before and after the UV light irradiation (350 nm with 40 mW cm<sup>-2</sup>) for 3 h at 300 K, which is shown in Fig. 6.32 [7(b)]. As shown in Fig. 6.32a, the <sup>57</sup>Fe Mössbauer spectra at 6 K before UV light irradiation shows two kinds of magnetically ordered states. The sextet with a large hyperfine field from -8 to +8 mm s<sup>-1</sup> is typical of the magnetically ordered spectrum of Fe<sup>III</sup>(t<sub>2g</sub><sup>3</sup>e<sub>g</sub><sup>2</sup>, S = 5/2) and the narrow quadrupole doublet at around 0.3 mm s<sup>-1</sup> is assigned to the diamagnetic Fe<sup>II</sup>(t<sub>2g</sub><sup>6</sup>, S = 0), which indicates the magnetically ordered LTP. The magnetic sextets of Fe<sup>II</sup>(t<sub>2g</sub><sup>4</sup>e<sub>g</sub><sup>2</sup>, S = 2) and Fe<sup>III</sup>(t<sub>2g</sub><sup>5</sup>, S = 1/2) corresponding to the HTP are also observed. However, as shown in Fig. 6.32b, after the UV light irradiation for 3 h at 300 K, the <sup>57</sup>Fe Mössbauer spectra corresponding to the LTP vanishes entirely at 6 K. In this way, the remarkable change of <sup>57</sup>Fe Mössbauer spectra derived from the UV light irradiation proves that the photo-isomerization of SP-Me<sup>+</sup> in (SP-Me)[Fe<sup>II</sup>Fe<sup>III</sup>(dto)<sub>3</sub>] induces the transformation from the phase (A) to the phase (B).

The photo-isomerization induced CTPT for (SP-Me)[Fe<sup>II</sup>Fe<sup>III</sup>(dto)<sub>3</sub>] is illustrated in Fig. 6.33. This new type of synergetic phenomenon coupled with spin, charge and photon is triggered by the photo-isomerization of intercalated spiropyran from the CF to the OF, which seems to have a significant similarity with the first event for



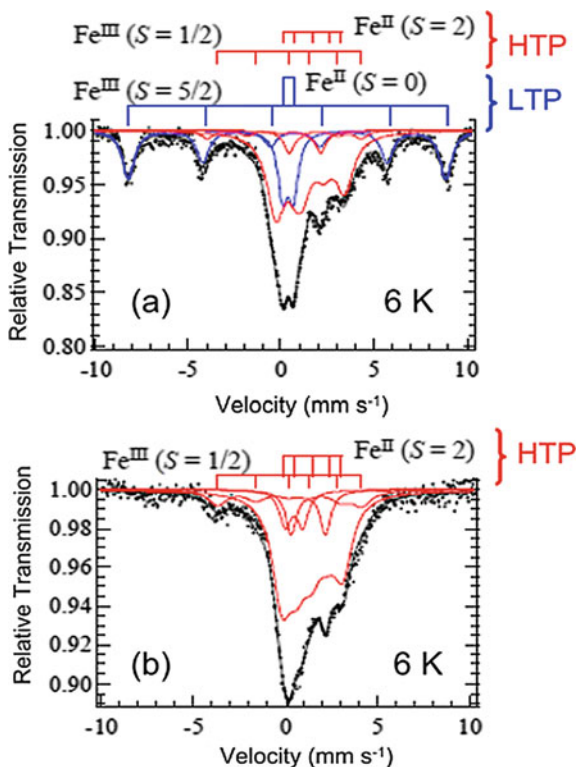


**Fig. 6.32**  $^{57}\text{Fe}$  Mössbauer spectra of  $(\text{SP-Me})[\text{Fe}^{\text{II}}\text{Fe}^{\text{III}}(\text{dto})_3]$  at 6 K before and after UV light irradiation ( $350\text{ nm}$  with  $40\text{ mW cm}^{-2}$ ) for 3 h at 300 K. Reprinted from [7(b)], Copyright 2009, with permission from Elsevier

the perception of light in rhodopsin where the photo-isomerization of 11-*cis*-retinal to the all-*trans*-retinal induces a conformational change in opsin and activates the associated G protein and triggers a second messenger cascade [51].

## 6.4 Single-Molecule Magnets and Single-Chain Magnets

### 6.4.1 Single-Molecule Magnets of Transition-Metal Clusters

Mössbauer spectroscopy have been applied to various kinds of molecular magnets as well as classical inorganic bulk magnets. Molecular magnets include not only classical magnets showing a long-range magnetic order but also quantum molecular magnets such as SMMs and SCMs the latter of which resemble superparamagnetic compounds in magnetism. These molecular nanomagnets have a possibility for

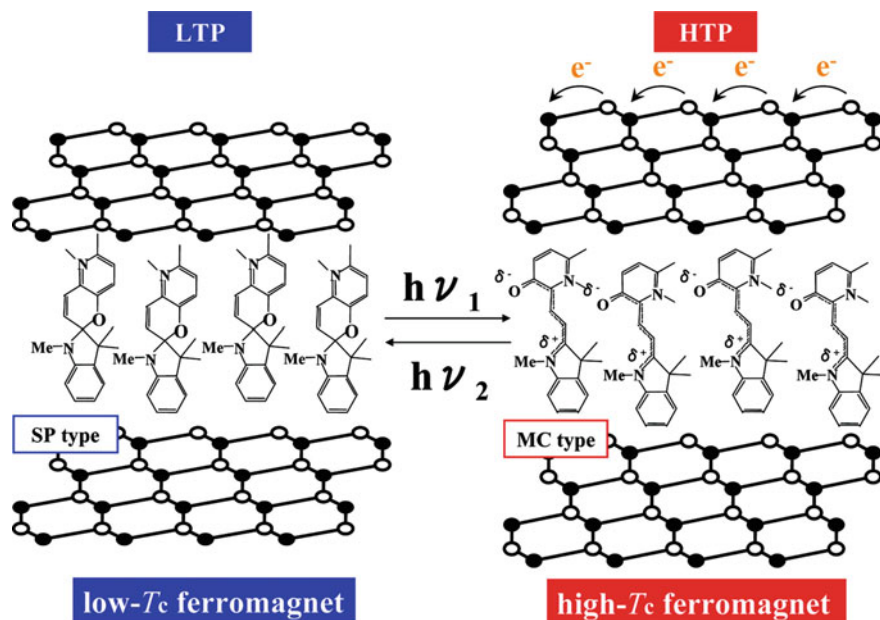


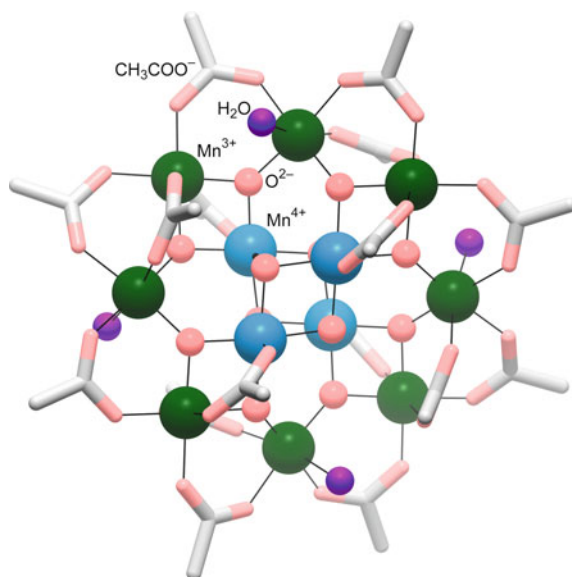
**Fig. 6.33** Schematic representation of the synergetic CTPT induced by the photo-isomerization of spiropyran in (SP-Me)[Fe<sup>II</sup>Fe<sup>III</sup>(dto)<sub>3</sub>]. White and black colored circles represent the Fe<sup>II</sup> and Fe<sup>III</sup> sites, respectively. Reprinted with permission from [7(a)]. Copyright 2009 American Chemical Society

ultra-high density memory, spintronics, and quantum computing devices. However, thermal and quantum relaxation processes limit them to afford such an application. Therefore, it is much important to elucidate slow relaxation dynamics of magnetization in quantum magnets. Varied measurements with individual time windows (Fig. 6.21) have been applied to SMMs and SCMs in order to reveal such spin dynamics. Especially, Mössbauer spectroscopy is a powerful tool to investigate spin dynamics for target atoms even in the condition of zero field as well as applied dc magnetic fields.

The dodecanuclear mixed-valence manganese cluster, [Mn<sub>12</sub>O<sub>12</sub>(AcO)<sub>16</sub>(H<sub>2</sub>O)<sub>4</sub>].2AcOH.4H<sub>2</sub>O (AcOH = acetic acid) abbreviated as [Mn<sub>12</sub>]<sub>ac</sub> (Fig. 6.34), is well known as the first SMM reported in 1993 [52], while the synthesis of [Mn<sub>12</sub>]<sub>ac</sub> had already been described in 1980 [53]. In the precedent papers, slow magnetization relaxation like superparamagnetic behavior was revealed in ac susceptibility measurements [54, 55], accompanied by that the nature of the ground spin state is shown to be  $S_{\text{total}} = 10$  by high-field electron paramagnetic resonance [54]. The relaxation time ( $\tau$ ) of magnetization was found to follow the Arrhenius law:

$$(\omega =) \frac{1}{\tau} = \frac{1}{\tau_0} \exp\left(-\frac{\Delta}{k_B T}\right), \quad (6.6)$$

**Fig. 6.34** Molecular structure of  $[\text{Mn}_{12}\text{O}_{12}(\text{AcO})_{16}(\text{H}_2\text{O})_4]$  ( $[\text{Mn}_{12}]_{\text{ac}}$ )



where  $\omega$  is the relaxation rate at the temperature of  $T$ ,  $1/\tau_0$  is the pre-exponential factor,  $\Delta$  is the effective activation energy, and  $k_B$  is the Boltzmann constant. This temperature dependence is the characteristics of the thermally-activated relaxation process by Orbach mechanism. The  $\Delta$  is corresponding to  $|D|S_z^2$  for an integer spin or  $|D|(S_z^2 - 1/4)$  for a half integer spin, where  $D$  represents the axial zero-field splitting parameter. For  $[\text{Mn}_{12}]_{\text{ac}}$ , the Arrhenius parameters were estimated as  $\tau_0 = 2.1 \times 10^{-7}$  s and  $\Delta/k_B = 61$  K [52], where the blocking temperature ( $T_B$ ) was estimated as about 3 K for  $\tau \sim 10^2$  s. Actually, magnetic hysteresis in  $MH$  curves was found below 4 K. Subsequently, some succeeding reports demonstrated clear magnetization steps (Fig. 6.35) in the hysteresis loops [56–58]. They are the first observations of quantum tunnelling of magnetization (QTM). A step occurs at every 0.44–0.46 T in an equally -spaced manner. The QTM originates in the level crossing between negative and positive  $m_S$  states as shown in Fig. 6.36. For example, at zero field the pair of  $+m_S$  and  $-m_S$  levels degenerates, affording a fast relaxation of magnetization because of the QTM. By applying external magnetic field, a non-zero field mismatching the energies of the  $+m_S$  and  $-m_S$  levels breaks down the tunnel relaxation. Some applied fields again lead to the degeneration of the energy levels when the  $m_S = +S$  level corresponds to the  $m_S = -S + n$  level ( $n$  is an integer), resulting in a fast relaxation. The interval field of the magnetization steps approximates the value of  $-nD/g\mu_B$ , giving the  $D$  value of  $\sim 0.60$  K for  $[\text{Mn}_{12}]_{\text{ac}}$ . From the Arrhenius analysis, the  $D$  value is given as 0.61 K using  $\Delta = |D|S_{\text{total}}^2$  ( $S_{\text{total}} = 10$ ), indicating an excellent agreement of those estimated values.

The  $[\text{Mn}_{12}]_{\text{ac}}$  has diversified into various derivatives, and wide variety of spectroscopic measurements have been performed to probe their SMM characteristics

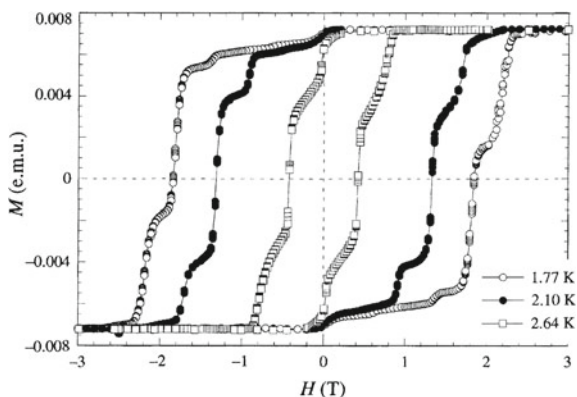


**Fig. 6.35** Magnetization versus magnetic field ( $MH$ ) curves at 1.77, 2.10, and 2.64 K for a single crystal (volume:  $0.066 \pm 0.008 \text{ mm}^3$ ) of  $[\text{Mn}_{12}]_{\text{ac}}$ . The magnetic field was applied along the magnetization axis, which aligns with the longest crystal dimension. Reprinted by permission from Springer Nature: [58], Copyright 1996

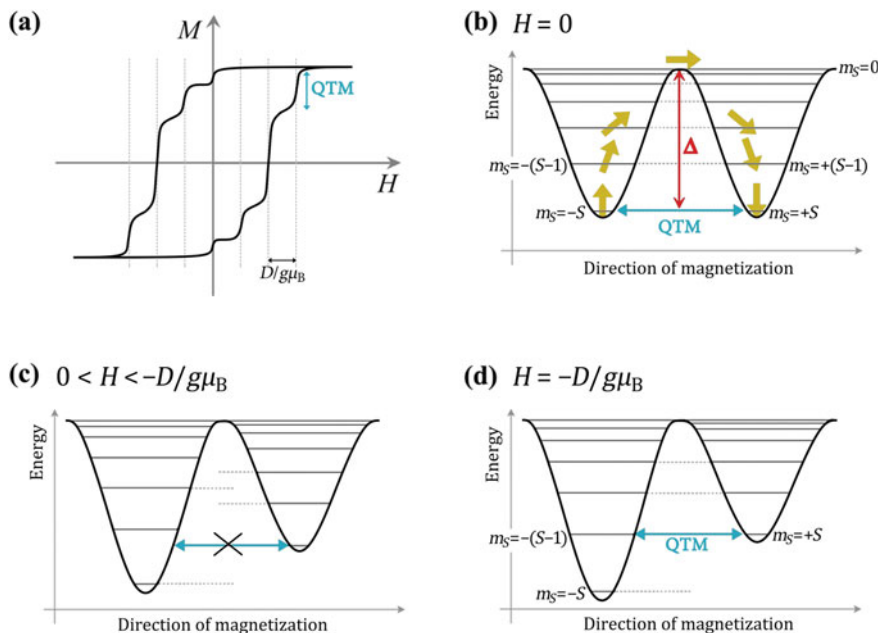


**Fig. 6.36** **a** Magnetic hysteresis curve and **b–d** double-well potentials with energy levels for a spin state of  $S$  for a single-molecule magnet having easy-axis magnetic anisotropy ( $D < 0$ ). The levels of positive  $m_S$  states are localized in the right well and the negative ones in the left well. Applied dc fields ( $H$ ) are **b** zero, **c**  $0 < H < -D/g\mu_B$ , and **d**  $-D/g\mu_B$ . The QTM occurs when energy levels between the two wells come to the same level

such as ground and excited spin states, magnetic anisotropy, and QTM. No Mössbauer study has been reported for  $[\text{Mn}_{12}]_{\text{ac}}$  because of less applicability for Mn atoms. A one-electron reduced analog,  $[\text{Fe}(\text{C}_5\text{H}_5)_2][\text{Mn}_{12}\text{O}_{12}(\text{O}_2\text{CC}_6\text{F}_5)_{16}(\text{H}_2\text{O})_4]$  ( $\text{Fe}(\text{C}_5\text{H}_5)_2 =$  ferrocenium cation), was reported by Kuroda et al. [59] to determine the relaxation of magnetization derived from the magnetic field of the  $[\text{Mn}_{12}]^-$  core via  $^{57}\text{Fe}$  Mössbauer spectra of the ferrocenium site. The complex showed the effective energy barrier ( $U_{\text{eff}}$ ) of magnetization reversal estimated as 50 K. In  $^{57}\text{Fe}$  Mössbauer spectra (Fig. 6.37) below 13.5 K, a broad magnetic hyperfine splitting was found, which is a proof of slow paramagnetic relaxation originating in the SMM behavior of the  $[\text{Mn}_{12}]^-$  unit.

The  $[\text{Fe}_4]$  [60, 61] and  $[\text{Fe}_8]$  [60, 62, 63] coordination clusters are representative SMMs, the chemical formulae of which represent as  $[\text{Fe}_4(\text{OCH}_3)_6(\text{dpm})_6]$  ( $\text{Hdpm} =$  dipivaloylmethane) and  $[\text{Fe}_8\text{O}_2(\text{OH})_{12}(\text{tacn})_6]\text{Br}_8$  (Fig. 6.38;  $\text{tacn} = 1,4,7-$

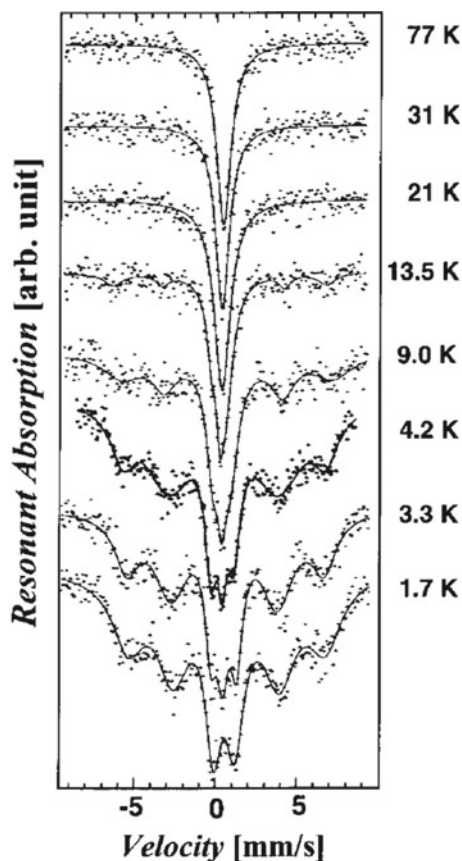


**Fig. 6.37** Temperature-varied  $^{57}\text{Fe}$  Mössbauer spectra of 11%  $^{57}\text{Fe}$ -enriched  $[\text{Fe}(\text{C}_5\text{H}_5)_2][\text{Mn}_{12}\text{O}_{12}(\text{O}_2\text{CC}_6\text{F}_5)_{16}(\text{H}_2\text{O})_4]$  sample [59]. Reprinted with permission from [59]. Copyright 2001 American Chemical Society

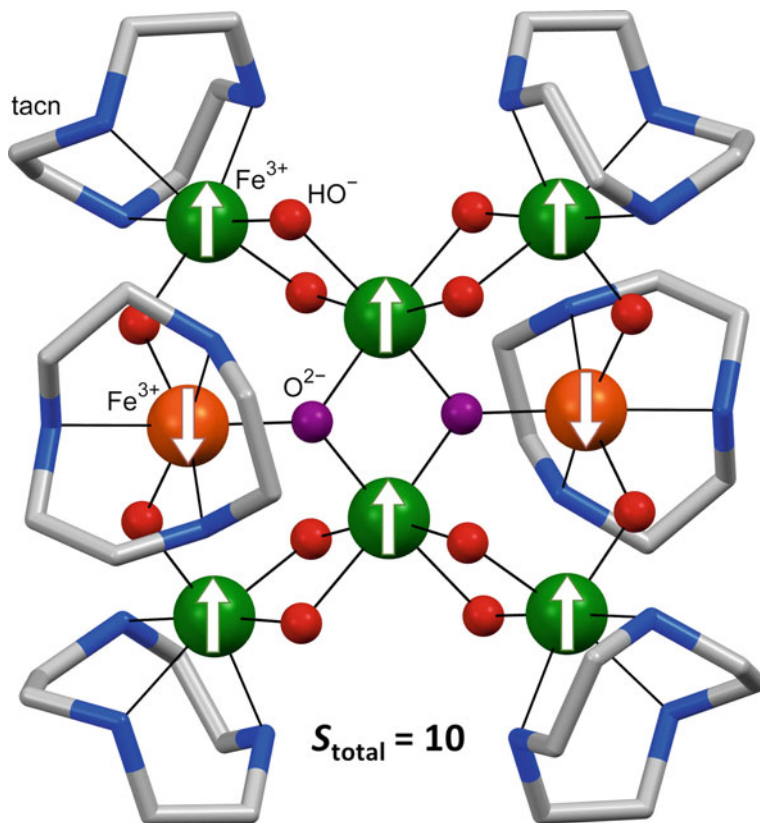
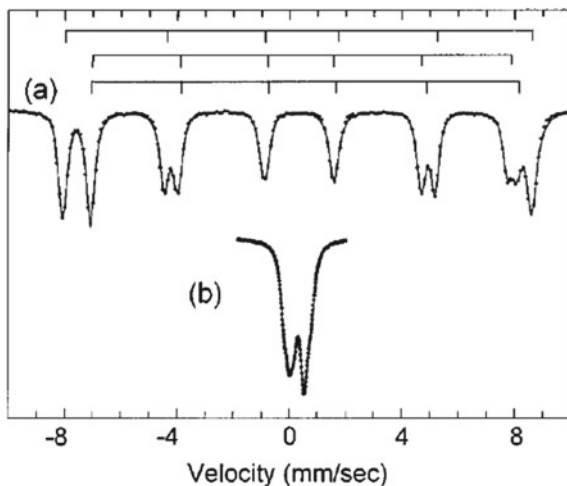


**Fig. 6.38** Molecular structure of  $[\text{Fe}_8\text{O}_2(\text{OH})_{12}(\text{tacn})_6]\text{Br}_8$ . The arrows represent the spin structure

triazacyclononane), respectively. These typical SMMs have been examined by means of  $^{57}\text{Fe}$  Mössbauer spectroscopy, which were well summarized in a preceding book [64].

The  $[\text{Fe}_8]$  complex consists of eight  $\text{Fe}^{\text{III}}$  ions to form the ground  $S_{\text{total}} = 10$  state [65] and shows SMM behavior with frequency dependence of ac magnetic susceptibilities giving  $\tau_0 = 1.9 \times 10^{-7}$  s and  $\Delta/k_{\text{B}} = 22.2$  K [63]. The relaxation time of magnetization was first investigated by means of  $^{57}\text{Fe}$  Mössbauer spectroscopy for a SMM. As shown in Fig. 6.39a, a clear magnetic sextet superimposed three six-line patterns was observed in the  $^{57}\text{Fe}$  Mössbauer spectrum at 2 K also under the absence of an external field. On heating, the splitting collapses gradually and results in partially-resolved quadrupole doublets at 300 K. A simplified line shape model was applied to the Mössbauer spectra in order to compare the estimated relaxation time with the values deduced from the ac magnetic measurements. The  $\tau$  values were reasonably evaluated as they are compatible with the Arrhenius law in the  $\ln(\tau)$  versus  $T^{-1}$  plot of ac measurements.

**Fig. 6.39**  $^{57}\text{Fe}$  Mossbauer spectra of  $[\text{Fe}_8]$  **a** at 2 K in an applied field of 0.22 T and **b** at 300 K in zero field. The rake-like bar graphs represent three sextet patterns attributable to the three iron sites. Reprinted with permission from [63]. Copyright 1987 EDP Sciences



Very recently, the development of synchrotron techniques enables us to employ  $^{57}\text{Fe}$  Mössbauer spectroscopy of a monolayer SMM grafted on a gold substrate. This technique was first applied to a monolayered sample containing a  $^{57}\text{Fe}$ -enriched  $[\text{Fe}_4]$  moiety [66], revealing slow magnetization relaxation of the iron cluster at zero magnetic field. In the monolayer, individual  $\text{Fe}^{\text{III}}$  sites lay in different chemical environments due to structural deformations induced by the interaction with the substrate, although such a modification tenuously affected SMM behavior. The zero-field splitting parameter,  $D$ , was estimated as  $|D| = -0.49(6)$  K by fitting  $^{57}\text{Fe}$  Mössbauer spectrum at the lowest temperature of 2.2 K, which is reduced compared to the typical values of  $\sim -0.6$  K for the  $[\text{Fe}_4]$  family.

## 6.4.2 Linear Two-Coordinate $\text{Fe}^{\text{II}}$ and $\text{Fe}^{\text{I}}$ Complexes

Linear two-coordinate  $\text{Fe}^{\text{II}}$  complexes have been recently developed in the viewpoint of remarkably slow magnetization relaxation to afford SMMs due to a large magnetic anisotropy. In particular, a species of SMM originated in magnetic anisotropy of a single metal ion are called single-ion magnets (SIMs). A representative two-coordinate  $\text{Fe}^{\text{II}}$  compound,  $[\text{Fe}(\text{C}(\text{SiMe}_3)_3)_2]$ , has impressed with a huge internal hyperfine field of 152 T in  $^{57}\text{Fe}$  Mössbauer spectra at 4.2 K on both chemists and physicists [66]. Such a giant magnetic anisotropy is attributable to the unquenched orbital angular momentum corresponding to the degenerate  $d_{xy} - d_{x^2-y^2}$  orbital pair. The  $[\text{Fe}(\text{C}(\text{SiMe}_3)_3)_2]$  compound possesses the strictly linear  $\text{C}-\text{Fe}^{\text{II}}-\text{C}$  geometry in the crystal [67, 68], being free from the Renner–Teller effect leading to a reduction of the orbital contribution due to a break of the local  $D_{\infty h}$  symmetry.

The  $^{57}\text{Fe}$  Mossbauer spectrum at room temperature shows an asymmetric doublet with much broadening in order to a magnetic relaxation, where the  $IS$  of  $\sim 0.4$  mm/s and the  $QS$  of 1.3 mm/s. The temperature-independent characteristics of quadrupole splitting is observed, indicating a large separation between the ground orbital states and the excited ones. Below about 50 K, the broad doublet becomes a well-resolved sextet, and then ends up with the sharp spectrum having overall hyperfine splitting of  $48.8$  mm s $^{-1}$  at 4.2 K. The result indicates slower magnetization relaxation than the Mössbauer time scale ( $\tau \sim 10^{-8}$  s). Magnetic hyperfine field,  $H_n$ , is estimated as 152 T. According to  $H_n = H_F + H_D + H_L$ , where  $H_F$  is the Fermi contact roughly determined by  $-12.7 \times (2S)$  T [69] and  $H_D$  is the dipolar contribution, the value of the orbital contribution term,  $H_L$ , is estimated as 203 T when  $H_D$  is assumed to be zero.

In the precedent paper [70], saturation magnetization of this compound was reported to reach  $\sim 32,500$  cm $^3$  Oe mol $^{-1}$  (or  $5.82 \mu_B$ ) at 1.85 K (for field-oriented sample), which is larger than the spin-only value ( $4 \mu_B$ ) that would be expected for the  $\text{Fe}^{\text{II}}$  ion with  $S = 2$ . After this preliminary study, the details of dynamic magnetization in the SIM compound have been examined by means of ac and dc magnetic property measurements and *ab initio* calculations [71], followed by the analysis of  $^{57}\text{Fe}$  Mössbauer relaxation spectra [72]. Low-temperature saturation magnetization for a fixed sample of  $[\text{Fe}(\text{C}(\text{SiMe}_3)_3)_2]$  is of  $M_{\text{sat}} = 3.24 \mu_B$ . This value is lower than the spin-only value of the HS  $\text{Fe}^{\text{II}}$  ion because of random orientation of strong anisotropic species. Actually, the  $\chi_M T$  value at room temperature is  $4.79$  cm $^3$  K mol $^{-1}$  (the effective magnetic moment:  $\mu_{\text{eff}} = 6.19 \mu_B$ ), indicating strong anisotropy with a large  $g$  value of 2.53. At zero applied dc field,  $[\text{Fe}(\text{C}(\text{SiMe}_3)_3)_2]$  shows no slow relaxation of magnetization in ac magnetic susceptibility, indicating no SIM behavior. However, such a relaxation can be detectable by means of  $^{57}\text{Fe}$  Mössbauer spectroscopy as shown in Fig. 6.40, and analysed using a relaxation model formalized by Dattagupta and Blume [73]. Relaxation time constant ( $\tau$ ) ranges from  $2.5 \times 10^{-7}$  to  $1.2 \times 10^{-10}$  s within the measuring temperature range of 5–295 K. From the analysis of Arrhenius plots, the physical parameters on quantum tunnelling and Orbach relaxation processes were extracted as  $\tau_{\text{QTM}}^{-1} = 4.2(3) \times 10^6$  s $^{-1}$  and  $U_{\text{eff}} = 178(9)$  and  $553(68)$  cm $^{-1}$ , respectively. Two obtained  $U_{\text{eff}}$  values correspond to the energy splitting from the ground  $M_J = \pm 4$  to the first excited  $M_J = \pm 3$  or the second excited  $M_J = \pm 2$  doublets among the Stark sublevels of  $^5\text{D}_4$ . It should be mentioned that ac susceptibility measurements ( $\tau < \sim 10^4$  s) cannot detect the magnetic relaxation for this system due to the fast QTM process ( $\tau_{\text{QTM}} = 2.4 \times 10^{-6}$  s) at the level crossing between the ground  $M_J = \pm 4$  states under zero field. Applying a small dc field induced suppression of the level crossing between the  $M_J$  doublets, and thus magnetization dynamics was observable as a nonzero signal in the out-of-phase ac susceptibility ( $\chi_M''$ ). For Cole–Cole plots, the relaxation dynamics can be evaluated by using a generalized Debye model [74, 75]. Their results reveal clearly the field-induced SIM nature of  $[\text{Fe}(\text{C}(\text{SiMe}_3)_3)_2]$ .

Following the pioneering compound, some of *ca.* 30 linear two-coordinate  $\text{Fe}^{\text{II}}$  complexes [76] have currently been investigated from the viewpoint of SIM



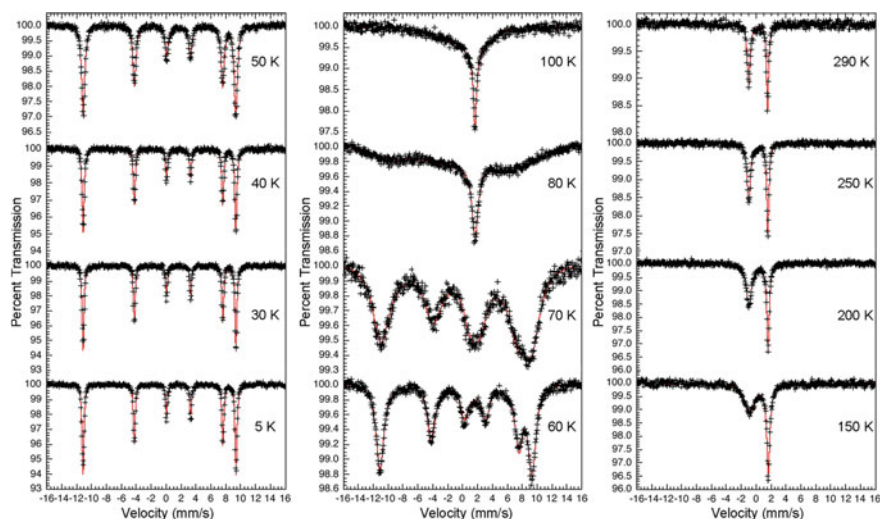


**Fig. 6.40** Temperature-varied  $^{57}\text{Fe}$  Mössbauer spectra of  $[\text{Fe}(\text{C}(\text{SiMe}_3)_3)_2]$  at zero dc magnetic field. Solid lines are the best fit profiles of a relaxation model. Reprinted with permission from [72]. Copyright 2013 American Chemical Society

behavior [71, 77, 78] as well as magnetization dynamics by using Mössbauer spectroscopy [78–81]. The development of linear two-coordinate metal complexes frequently needs the introduction of bulky ligands. A fused-ring 1,1,3,3,5,5,7,7-octa-*R*-substituted *s*-hydrindacene skeleton (Rind) is useful as a sterically-hindered ligand to isolate stably low-coordinated complexes [82]. Linear two-coordinate iron(II) complexes with various Rinds have been developed and investigated for an extremely large internal hyperfine field in the Mössbauer spectrum [78]. Owing to bulkiness of ligands, the crystal structure of  $\text{Fe}(\text{Eind})_2$  (Fig. 6.41; Eind denotes Rind of  $R = \text{ethyl}$ ) adopts a highly linear two-coordinate geometry with the  $\text{C}-\text{Fe}-\text{C}$  bond angles of  $174.24(15)$ – $177.73(13)^\circ$ . The effective magnetic moment of  $5.82 \mu_{\text{B}}$  at 300 K exceeds the spin-only value of  $4.90 \mu_{\text{B}}$  estimated for a HS ( $S = 2$ )  $\text{Fe}^{\text{II}}$  species, indicating virtually unquenched orbital angular momentum on the 3d electrons of  $\text{Fe}^{\text{II}}$ .

Such a large contribution of angular momentum leads to slow magnetization reversal, which is detectable by means of ac magnetic measurements (about 10–1000 Hz) as well as  $^{57}\text{Fe}$  Mössbauer spectroscopy. Without a dc magnetic field, no frequency dependence was observed in the ac magnetic susceptibilities, which is consistent with a broad signal derived from paramagnetic relaxation in the  $^{57}\text{Fe}$  Mössbauer spectrum at 4.2 K. This Mössbauer result indicates that the relaxation time approaches the time scale of  $10^{-9}$  s. The rapid relaxation is due to QTM. An applied dc field of 0.1 T suppressed the quantum tunnelling effectively, and consequently the spectrum split into a remarkably wide sextet with an internal hyperfine field of  $H_n = 140.3$  T. The  $H_n$  value reached up to 143.1 T at an applied field of 3.0 T. The  $IS$  is  $0.368(9) \text{ mm s}^{-1}$  and  $QS = -1.706(13) \text{ mm s}^{-1}$ . The  $QS$  value is rather

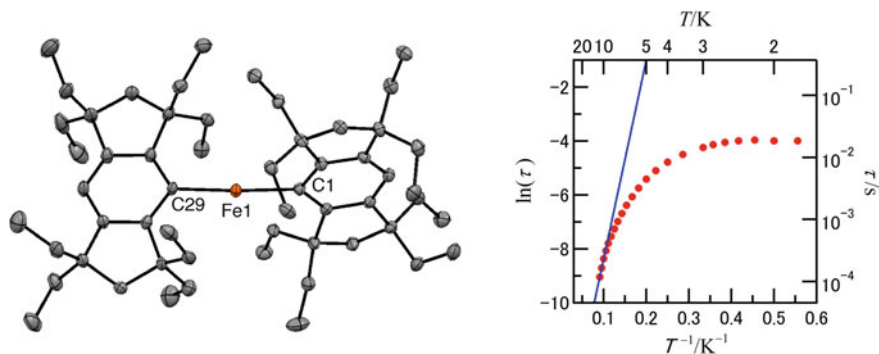


**Fig. 6.41** (left) Crystal structure of  $\text{Fe}(\text{Eind})_2$  with 50% probability ellipsoids. Hydrogen atoms are omitted for clarity. (right) Arrhenius plot showing the temperature dependence of the relaxation time ( $\tau$ ). The solid line represents a data fit to the Arrhenius law. Reprinted with permission from [78]. Copyright 2016 the Chemical Society of Japan

negative, reflecting a larger electric field gradient at the iron(II) ion compared with that of  $[\text{Fe}(\text{C}(\text{SiMe}_3)_3)_2]$  showing  $QS = -1.08(1)$  to  $-1.27 \text{ mm s}^{-1}$ . As with  $^{57}\text{Fe}$  Mössbauer results, slow relaxation was observed in the  $\chi_M''$  versus frequency plots below 12 K in the ac frequency range of 5–1512 Hz with the applied dc field of 1200 Oe. The analysis of Arrhenius plots (Fig. 6.41) gave  $U_{\text{eff}} = 51.2(7) \text{ cm}^{-1}$ . At lower temperatures ( $T < 10 \text{ K}$ ), a dominant relaxation process gradually changed from thermally-activated Orbach mechanism to direct and/or Raman ones before quantum tunnelling regime in the temperature range less than 3 K.

Very recently, the first two-coordinate  $\text{Fe}^{\text{I}}$  complex,  $[\text{Fe}^{\text{I}}(\text{C}(\text{SiMe}_3)_3)_2]^-$ , was developed via the chemical reduction of  $[\text{Fe}^{\text{II}}(\text{C}(\text{SiMe}_3)_3)_2]^0$  using  $\text{KC}_8$ , and its excellent SIM behavior was reported [83]. This complex has a highly anisotropic  $S = 3/2$  spin state that is regarded as a Kramers ion with the ground  $M_J = \pm 7/2$  doublets. Single-crystal X-ray diffraction analysis revealed the almost perfectly linear structure with the C–Fe–C angle of  $179.2(2)^\circ$  [83]. Extremely slow magnetization relaxation to behave as SIM was observed in the absence of an applied dc field, resulting in a large magnetic hysteresis loop due to magnetic blocking below 4.5 K. The effective activation barrier of spin reversal is estimated as  $U_{\text{eff}} = 226(4) \text{ cm}^{-1}$  from ac susceptibility measurements, which is consistent with the value of  $U_{\text{eff}} = 246(3) \text{ cm}^{-1}$  evaluated by the analyses of  $^{57}\text{Fe}$  Mössbauer relaxation spectra [72].

### 6.4.3 Single-Chain Magnets: Unique Chain Magnet with Easy-Plane Anisotropy

Although pure one-dimensional (1D) spin systems never show magnetic phase transition based on any long-range ordering at a finite temperature, they can afford

to behave like a magnet below a blocking temperature in the case of the presence of strong uniaxial magnetic anisotropy. Such compounds are categorized as SCMs, where slow relaxation dynamics of magnetization follows the Arrhenius law [Eq. (6.6)]. Dynamics of spin reversal for Ising chain systems is formulated by Glauber [84], whose model manages to explain quantitatively experimental results for some tangible SCMs. There are currently some practical reviews for SCMs [85, 86], interpreting anisotropic Heisenberg model applicable to the real materials, based on Glauber dynamics of 1D Ising chain. The spin system can be described by the following Hamiltonian:

$$H = -2J \sum_{i=1}^L S_i \cdot S_{i+1} + D \sum_{i=1}^L S_i^2 - g\mu_B H \sum_{i=1}^L S_i^2, \quad (6.7)$$

where  $J$  is the exchange coupling constant between adjacent spins and  $L$  the effective chain length. In the case of  $|D/J| > 4/3$  (Ising limit), the spin system can be considered to be pseudo-Ising chain as shown in Fig. 6.42. At finite temperatures, the thin domain walls are created with the energy barrier  $2\Delta_\xi = 8|J|S^2$  if the system is regarded as the infinite chain with the small domain size ( $2\xi$ ) compared to  $L$  (that is  $2\xi < L$ , Fig. 6.42a). Additionally, each spin has an anisotropic energy of  $\Delta_A = |D|S^2$ , and therefore the relaxation time can be described as follows,

$$\tau_1 = \tau_0 \exp\left(\frac{2\Delta_\xi + \Delta_A}{k_B T}\right) = \tau_0 \exp\left(\frac{(8J + |D|)S^2}{k_B T}\right). \quad (6.8)$$

On cooling,  $\xi$  increases exponentially and gets comparable to  $L$ , which results in the occurrence of the finite size effect (Fig. 6.42b). In such a case, the formation

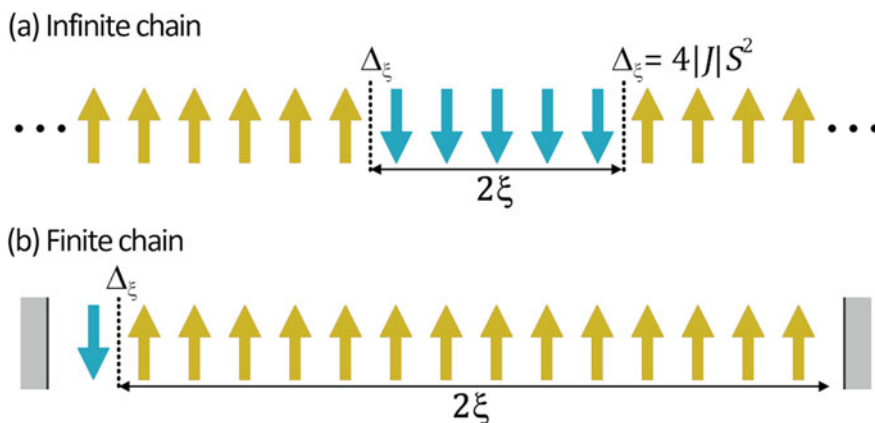


**Fig. 6.42** Schematic represents for spin reversal in **a** infinite and **b** finite Ising chain systems. The parameters of  $\Delta_\xi$  and  $\xi$  denote the energy barrier of spin reversal and the correlation length ( $2\xi$ : the width of domain), respectively

energy of the domain is  $\Delta_{\xi} = 4|J|S^2$  due to the creation of the domain wall in only one side. Thus, the thermal activation energy can be estimated as  $(4J + |D|)S^2$ , and the dynamics of magnetization reversal obeys Eq. (6.9).

$$\tau_2 = \tau_0 \exp\left(\frac{\Delta_{\xi} + \Delta_A}{k_B T}\right) = \tau_0 \exp\left(\frac{(4J + |D|)S^2}{k_B T}\right) \quad (6.9)$$

In 2001, a slow relaxation of magnetization like SMMs was observed in 1D spin systems. The first SCM is the metal-radical compound [Co(hfac)<sub>2</sub>(NITPhOMe)] (Hhfac = hexafluoroacetylacetonate, NITPhOMe = *p*-methoxyphenyl nitronyl nitroxide) [87]. This compound consists of the effective  $S = 1/2$  spin of Co<sup>2+</sup> ( $g_{\text{Co}} = 7.4$ ) and the  $S = 1/2$  spin of radical ( $g_{\text{R}} = 2$ ) connected via an antiferromagnetic coupling ( $2J/k_B = -220$  K for  $-2J\Sigma S_{\text{Co}} \cdot S_{\text{R}}$ ). The ac measurements revealed frequency dependences of  $\chi_M'$  and  $\chi_M''$  below 17 K, indicating apparently a slow relaxation of magnetization. The relaxation time was perfectly accordance with the Arrhenius law, and the analysis gave the parameters of  $\tau_0 = 3.0(2) \times 10^{-11}$  s and  $\Delta/k_B = 154(2)$  K.

Almost coincidentally, a heterometallic chain [Mn<sub>2</sub>(saltmen)<sub>2</sub>Ni(pao)<sub>2</sub>(py)<sub>2</sub>](ClO<sub>4</sub>)<sub>2</sub> (H<sub>2</sub>saltmen = *N,N'*-bis(salicylidene)tetramethylethylenediamine, Hpao = pyridine-2-aldoxime) was developed in 2002 [87], which is comprised of ferromagnetically-coupled  $S_T = 3$  spin units to form an Ising-like chain. Varied magnetic analyses were performed to scrutinize Glauber dynamics for the compound [88, 89]. Below 6.5 K, the frequency dependence of  $\chi_M'$  and  $\chi_M''$  were clearly observed, and a semicircle in the Cole–Cole plot indicates a practical single relaxation process according to the Debye model. From a detailed Arrhenius plot, such a thermally-activated relaxation process switched in the vicinity of  $\sim 2.7$  K (Fig. 6.43). The Arrhenius parameters of two relaxation manners were given as  $\tau_0 = 5.5(1) \times 10^{-11}$  s,  $\Delta_1/k_B = 72(1)$  K in a high-temperature region and  $\tau_0 \sim 10^{-8}$  s,  $\Delta_2/k_B \sim 55$  K in a low-temperature one. The former is considered as the infinite chain regime according to Eq. (6.8), and the latter seems to obey Eq. (6.9) due to the finite size effect. The exchange coupling between the spin units was estimated as  $J/k_B = 0.77$  K by means of dc magnetic measurements, while the anisotropy parameter of each unit was  $D/k_B = -2.5$  K. The  $\Delta_1$  and  $\Delta_2$  are excellent consistent with the expected values of  $(8J + |D|)S_T^2$  ( $= 78$  K) and  $(4J + |D|)S_T^2$  ( $= 50$  K), respectively.

Among various SCMs developed, there are few examples on Mössbauer relaxation study compared with an overwhelming number of ac susceptibility measurements. An alternating Fe<sup>II</sup>–Fe<sup>III</sup> chain compound, *catena*-[Fe<sup>II</sup>(ClO<sub>4</sub>)<sub>2</sub>{Fe<sup>III</sup>(bpc)<sub>2</sub>}]ClO<sub>4</sub> (Hbpc = bis(2-pyridylcarbonyl)amine) as shown in Fig. 6.44, is one of representative SCMs, where <sup>57</sup>Fe Mössbauer and  $\mu$ SR spectroscopic measurements were performed to investigate the spin relaxation based on Glauber dynamics in the chain structure [90, 91]. The material can be described as a unique 1D Ising system composed of metal ions in the nature of easy-plane magnetic anisotropy ( $D > 0$ ). In general, SMMs and SCMs prefer consisting of an easy-axis anisotropic ( $D < 0$ ) metal ions in order to overcome a thermal relaxation of magnetization. However, the overall easy-axis anisotropy of the molecule can stem from the

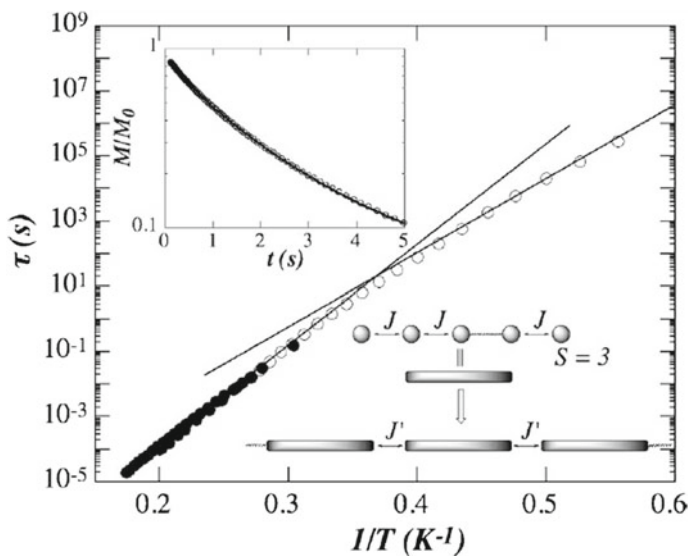


**Fig. 6.43** Arrhenius plot of the relaxation time  $\tau$  (logarithmic scale) versus  $1/T$ . Inset graph is time-dependent magnetization relaxation at 3 K. Solid lines represent the best fits using the model for Glauber dynamics. Schematic view indicates the spin model consisting of  $S = 3$  units connected by an inter-unit ferromagnetic coupling of  $J'$ . Reprinted figure with permission from [89]. Copyright 2004 by the American Physical Society

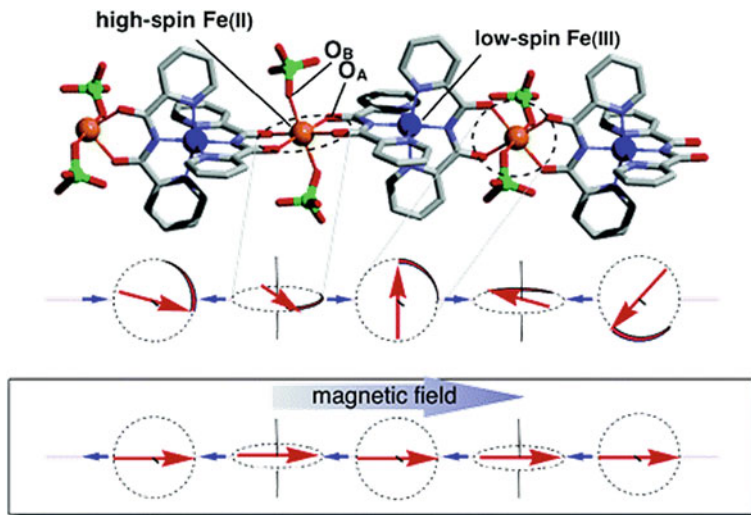


**Fig. 6.44** Crystal structure of the *catena*- $[\text{Fe}^{\text{II}}(\text{ClO}_4)_2\{\text{Fe}^{\text{III}}(\text{bpca})_2\}]\text{ClO}_4$  (Hbpca = bis(2-pyridylcarbonyl)amine) and the spin alignment of  $\text{Fe}^{\text{II}}$  ( $S = 2$ )– $\text{Fe}^{\text{III}}$  ( $S = 1/2$ ) in the chain. Reprinted with permission from [90]. Copyright 2005 American Chemical Society

orthogonal arrangement of each metal ion with easy-plane anisotropy. In *catena*-[Fe<sup>II</sup>(ClO<sub>4</sub>)<sub>2</sub>{Fe<sup>III</sup>(bpca)<sub>2</sub>}]ClO<sub>4</sub>, the HS Fe<sup>II</sup> ions have a octahedral coordination geometry with the axial bonds elongated. This situation can provides an easy-plane anisotropy (XY spin) in the equatorial plane. The XY spin of each Fe<sup>II</sup> site is coupled antiferromagnetically with Fe<sup>III</sup> ( $S = 1/2$ ) spins in an alternately-twisted array of the easy-plane, which affords a net easy-axis anisotropy along the chain direction. This compound showed a slow magnetization relaxation in ac susceptibility, and activation energy  $U_{\text{eff}}/k_{\text{B}}$  of 27 K was estimated from the Arrhenius plot [90]. The  $U_{\text{eff}}$  value is smaller than the  $(8J + |D|)S^2$  expected for pure Glauber dynamics theory, suggesting that the transverse magnetization of the Fe<sup>II</sup> spins in the easy plane is responsible for the magnetic relaxation.

A short-range ordering was observed in <sup>57</sup>Fe Mössbauer spectroscopy as well as  $\mu$ SR spectroscopy [91]. The  $\mu$ SR technique is one of the methods to approach a ground magnetic state at zero field (ZF). The depolarization of spin-polarized muons was observed in ZF- $\mu$ SR time spectra at 20 K, which are reproducible by using two Gaussian-type relaxations. On cooling down to 6 K, a gradual loss of the initial asymmetry was found, which was simultaneously followed by the enhancement of the relaxation rate for the fast depolarizing component. Below 6 K, the initial asymmetry became almost constant, and the relaxation rate declined rapidly after the divergence around 6 K. This behavior indicates a critical slowing down of magnetic fluctuation. No oscillation signal was observed in the decay spectra even at 0.3 K, indicating that the muon is located in a randomly distributed magnetic field.

The <sup>57</sup>Fe Mössbauer spectroscopy also accepts a short-range ordering nature of magnetic moment on the SCM compound (Fig. 6.45). Above 20 K, two doublets are

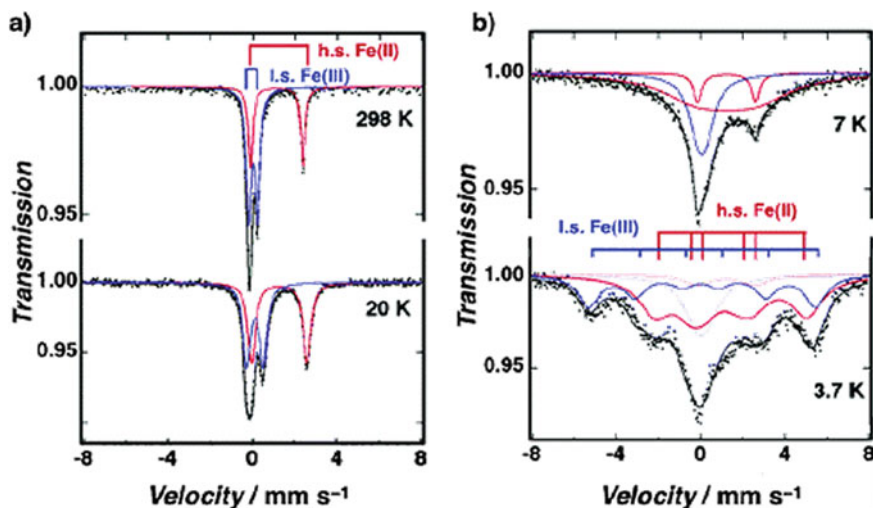


Fig. 6.45 Temperature-varied <sup>57</sup>Fe Mössbauer spectra of *catena*-[Fe<sup>II</sup>(ClO<sub>4</sub>)<sub>2</sub>{Fe<sup>III</sup>(bpca)<sub>2</sub>}]ClO<sub>4</sub> **a** at 298 and 20 K, **b** at 7 and 3.7 K. Reprinted with permission from [90]. Copyright 2005 American Chemical Society

observed, which are assignable as the HS Fe<sup>II</sup> and LS Fe<sup>III</sup> species. These paramagnetic signals turn into broadening before splitting into two magnetic sextet with a partially residual paramagnetic components below 7 K. The hyperfine fields were estimated at 19.2 T for Fe<sup>II</sup> and 33.5 T for Fe<sup>III</sup>.

## 6.5 Conclusion

In this chapter, we have focused on the molecular magnetism and its related light-induced phase transitions from the viewpoint of Mössbauer spectroscopy. In the Sect. 6.2, we have described mainly the dynamic spin equilibrium phenomena for [M<sup>II</sup>Fe<sup>III</sup>(mto)<sub>3</sub>] (M = Zn, Mn) complexes. In the case of (C<sub>6</sub>H<sub>5</sub>)<sub>4</sub>P[Mn<sup>II</sup>Fe<sup>III</sup>(mto)<sub>3</sub>] consisting of Fe<sup>III</sup>O<sub>3</sub>S<sub>3</sub> and Mn<sup>II</sup>O<sub>6</sub> octahedra, there exists a rapid spin equilibrium ( $\tau < 10^{-7}$  s) between the HS and LS states at the Fe<sup>III</sup>O<sub>3</sub>S<sub>3</sub> site, which induces the fluctuation of internal magnetic field on the Mn<sup>II</sup> site. Owing to the fluctuation of internal magnetic field caused by the rapid spin equilibrium, (C<sub>6</sub>H<sub>5</sub>)<sub>4</sub>P[Mn<sup>II</sup>Fe<sup>III</sup>(mto)<sub>3</sub>] undergoes the successive magnetic phase transitions at 30 and 23 K. In the Sect. 6.3, we have described the CTPT and the ferromagnetism of (n-C<sub>n</sub>H<sub>2n+1</sub>)<sub>4</sub>N[Fe<sup>II</sup>Fe<sup>III</sup>(dto)<sub>3</sub>]. At the CTPT, the electrons of Avogadro's constant transfer between the Fe<sup>II</sup> and Fe<sup>III</sup> sites, and the Fe valence state is dynamically fluctuated with a frequency of about 0.1 MHz, which was confirmed by means of  $\mu$ SR. In order to control the ferromagnetism and the CTPT by means of photo-irradiation, we have synthesized a photo-responsive organic-inorganic hybrid system, (SP-Me)[Fe<sup>II</sup>Fe<sup>III</sup>(dto)<sub>3</sub>], and discovered that the photo-isomerization of intercalated SP-Me by UV light irradiation induces the CTPT and the enhancement of the Curie temperature from 7 to 22 K. In the Sect. 6.4, we have described the spin dynamics of various kinds of molecular magnets such as SMMs with transition-metal clusters, SIMs with linear coordination, and SCMs with easy-plane anisotropy.

**Acknowledgements** In this chapter, our contributed original research has been created in collaboration with Profs. M. Enomoto (Tokyo University of Science), M. Itoi (Nihon University), M. Okubo (The University of Tokyo), K. Kagesawa (Tohoku University), T. Matsuo (Kinki University), Y. Kobayashi (University of Electro-Communications), T. Kajiwara (Nara Women's University), K. Tamao (Toyota Riken), M. Yamashita (Tohoku University), M. Seto (Kyoto University), H. Sawa (Nagoya University), E. Nishibori (Tsukuba University), Drs. N. Kida (Mitsubishi Chemical Co.), Y. Ono (Mitsubishi Chemical Co.), I. Watanabe (RIKEN). We wish to thank all the collaborators. This work has partly been supported by Toyota Physical and Chemical Research Institute, and a Grant-in-Aid for Science Research from the Ministry of Education, Science, Sports and culture.

## References

1. (a) P. Gülich, H.A. Goodwin (Ed.), *Spin Crossover in Transition Metal Compounds I, II, III* (Springer, 2004). (b) M.A. Halcrow (Ed.), *Spin-Crossover Materials: Properties and Applications* (Wiley, 2013). (c) J.-P. Launay, M. Verdaguer, *Electronics in Molecules: From Basic Principles to Molecular Electronics* (Oxford University Press, 2013). (d) D. Gatteschi, R. Sessoli, J. Villain, *Molecular Nanomagnets* (Oxford University Press, 2006). (e) R. Winpenny, G. Aromi (Ed.), *Single-Molecule Magnets and Related Phenomena* (Springer, 2006). (f) M. Holynska (Ed.), *Single-Molecule Magnets: Molecular Architectures and Building Blocks for Spintronics* (Wiley, 2018)
2. (a) N. Kojima, M. Enomoto, N. Kida, K. Kagesawa, *Materials*, **3**, 3141 (2010). (b) N. Kojima, M. Itoi, Y. Miyazaki, *Curr. Inorg. Chem.* **4**, 85 (2014). (c) N. Kojima, A. Sugahara, Spin-crossover and related phenomena coupled with spin, photon and charge, in *Mössbauer Spectroscopy: Applications in Chemistry, Biology and Nanotechnology*. ed. by V.K. Sharma, C. Klingelhöfer, T. Nishida (Wiley Inc., 2013), pp. 152–176
3. K. Kagesawa, A. Okazawa, M. Enomoto, N. Kojima, *Chem. Lett.* **39**, 872 (2010)
4. N. Kojima, W. Aoki, M. Itoi, M. Seto, Y. Kobayashi, Yu. Maeda, *Solid State Commun.* **120**, 165 (2001)
5. N. Kida, M. Enomoto, I. Watanabe, T. Suzuki, N. Kojima, *Phys. Rev. B* **77**, 144427 (2008)
6. M. Itoi, Y. Ono, N. Kojima, K. Kato, K. Osaka, M. Takata, *Eur. J. Inorg. Chem.* 1198 (2006)
7. (a) N. Kida, M. Hikita, I. Kashima, M. Okubo, M. Itoi, M. Enomoto, K. Kato, M. Takata, N. Kojima, *J. Am. Chem. Soc.* **131** 212 (2009). (b) N. Kida, M. Hikita, I. Kashima, M. Enomoto, M. Itoi, N. Kojima, *Polyhedron* **28**, 1694 (2009)
8. Y. Tanabe, S. Sugano, *J. Phys. Soc. Jpn.* **9**, 766 (1954)
9. (a) L. Cambi, A. Cagnasso, *Atti Accad. Naz. Lincei.* **13** 809 (1931). (b) L. Cambi, L. Szegö, A. Cagnasso, *Atti Accad. Naz. Lincei.* **15**, 266 (1932). (c) L. Cambi, L. Szegö, *Ber. Deutsch. Chem. Ges.* **66**, 656 (1933)
10. J.M. Fiddy, I. Hall, F. Gradjean, U. Russo, G.J. Long, *Inorg. Chem.* **26**, 4138 (1987)
11. (a) K.R. Kunze, D.L. Perry, L.J. Wilson, *Inorg. Chem.* **16**, 594 (1977). (b) H. Oshio, Y. Maeda, Y. Takahashi, *Inorg. Chem.* **22**, 2684 (1983). (c) Y. Maeda, N. Tsutsumi, Y. Takahashi, *Inorg. Chem.* **23**, 2440 (1984). (d) M.D. Timken, A.M. Abdel-Mawgoud, D.N. Hendrickson, *Inorg. Chem.* **25**, 160 (1985). (e) M. Nihei, T. Shiga, Y. Maeda, H. Oshio, *Coord. Chem. Rev.* **251**, 2606 (2007)
12. W.A. Baker, H. Bobonich, *Inorg. Chem.* **3**, 1184 (1964)
13. P. Gülich, H.A. Goodwin (Ed.), *Spin Crossover in Transition Metal Compounds I* (Springer-Verlag, Berlin Heidelberg, Germany, 2004), and related references therein
14. (a) I. Krivokapic, M. Zerara, M.L. Daku, A. Vargas, C. Enachescu, C. Ambrus, P. Tregenna-Piggott, N. Amstutz, E. Krausz, A. Hauser, *Coord. Chem. Rev.* **251**, 364 (2007). (b) H.A. Goodwin, in *Spin Crossover in Transition Metal Compounds II*, ed. by P. Gülich, H.A. Goodwin (Springer-Verlag, Berlin Heidelberg, Germany, 2004), pp. 23–48
15. Y. Garcia, P. Gülich, in *Spin Crossover in Transition Metal Compounds II*, ed. by P. Gülich, H.A. Goodwin (Springer-Verlag, Berlin Heidelberg, Germany, 2004), pp. 49–62
16. (a) P.L. Franke, J.G. Haasnoot, A.P. Zuur, *Inorg. Chim. Acta* **59**, 5 (1982). (b) S. Decurtins, P. Gülich, C.P. Köhler, H. Spiering, A. Hauser, *Chem. Phys. Lett.* **105**, 1 (1984). (c) S. Decurtins, P. Gülich, K.M. Hasselbach, A. Hauser, H. Spiering, *Inorg. Chem.* **24**, 2174 (1985)
17. (a) P. Gülich, H.A. Goodwin (Ed.) *Spin Crossover in Transition Metal Compounds I, II, III*, (Springer-Verlag, Berlin Heidelberg, Germany, 2004). (b) O. Sato, J. Tao, Y.-Z. Zhang, *Angew. Chem. Int. Ed.* **46**, 2152 (2007), and related references therein
18. M. Cox, J. Darken, B.W. Fitzsimmons, A.W. Smith, L.F. Larkworthy, K.A. Rogers, *J. Chem. Soc. Dalton Trans.* 1192 (1972)
19. K.R. Kunze, D.L. Perry, L.J. Wilson, *Inorg. Chem.* **16**, 594 (1977)
20. M. Itoi, A. Taira, M. Enomoto, N. Matsushita, N. Kojima, Y. Kobayashi, K. Asai, K. Koyama, T. Nakamoto, Y. Uwatoko, J. Yamamura, *Solid State Commun.* **130**, 415 (2004)



21. H. Ôkawa, N. Matsumoto, H. Tamaki, M. Ohba, *Mol. Cryst. Liq. Cryst.* **233**, 257 (1993)
22. A. Hauser, in *Spin Crossover in Transition Metal Compounds II*, ed. by P. Gütllich, H.A. Goodwin (Springer-Verlag, Berlin Heidelberg, Germany, 2004), pp. 155–198
23. T.C. Brunold, H.U. Güdel, in *Inorganic Electronic Structure and Spectroscopy I*, ed. by E.I. Solomon, A.B.P. Lever (Wiley, 1999), pp. 259–306
24. (a) J.-F. Létard, G. Chastanet, P. Guionneau, C. Desplanches, in *Spin-Crossover Materials: Properties and Applications*, ed. by M.A. Halcrow (Wiley, 2013), pp. 475–506. (b) Y. Moritomo, K. Kato, A. Nakamoto, N. Kojima, E. Nishibori, M. Takata, M. Sakata, *J. Phys. Soc. Jpn.* **71**, 1015 (2002)
25. (a) S.G. Carling, J.M. Bradley, D. Visser, P. Day, *Polyhedron* **22**, 2317 (2003). (b) M. Enomoto, H. Ida, A. Okazawa, N. Kojima, *Crystals* **8**, 446 (2018)
26. C. Mathonière, C.J. Nuttall, S.G. Carling, P. Day, *Inorg. Chem.* **35**, 1201 (1996)
27. K. Kagesawa, Doctoral Thesis, (The University of Tokyo, 2011)
28. M.B. Robin, P. Day, *Adv. Inorg. Chem. Radiochem.* **10**, 247 (1967)
29. F. Herren, P. Fischer, A. Ludi, W. Hälgl, *Inorg. Chem.* **19**, 956 (1980)
30. A. Ito, M. Suenaga, K. Ôno, *J. Chem. Phys.* **48**, 3597 (1968)
31. K. Maer Jr., M.L. Beasley, R.L. Collins, W.O. Milligan, *J. Am. Chem. Soc.* **90**, 3201 (1968)
32. O. Sato, T. Iyoda, A. Fujishima, K. Hashimoto, *Science* **272**, 704 (1996)
33. O. Sato, Y. Einaga, T. Iyoda, A. Fujishima, K. Hashimoto, *J. Electrochem. Soc.* **144**, L11 (1967)
34. O. Sato, J. Tao, Y.-Z. Zhang, *Angew. Chem. Int. Ed.* **46**, 2152 (2007), and related references therein
35. O. Sato, Y. Einaga, T. Iyoda, A. Fujishima, K. Hashimoto, *J. Phys. Chem. B* **101**, 3903 (1997)
36. (a) N. Shimamoto, S. Ohkoshi, O. Sato, K. Hashimoto, *Inorg. Chem.* **41**, 678 (2002). (b) V. Escax, A. Bleuzen, C. Cartier dit Moulin, F. Villain, A. Goujon, F. Varret, M. Verdager, *J. Am. Chem. Soc.* **123**, 12536 (2001). (c) A. Carolina, G.H. Matthew, P. Andrey, S. Codi, S. Darryl, R.D. Kim, *J. Am. Chem. Soc.* **132**, 13123 (2010). (d) H. Tokoro, S. Ohkoshi, T. Matsuda, K. Hashimoto, *Inorg. Chem.* **43**, 5231 (2004). (e) A. Bleuzen, V. Marvaud, C. Mathoniere, B. Sieklucka, M. Verdager, *Inorg. Chem.* **48**, 3453 (2009). (f) S. Ohkoshi, Y. Hamada, T. Matsuda, Y. Tsunobuchi, H. Tokoro, *Chem. Mater.* **20**, 3048 (2008). (g) R. Podgajny, S. Chorazy, W. Nitek, M. Rams, A.M. Majcher, B. Marszalek, J. Zukrowski, C. Kapusta, B. Sieklucka, *Angew. Chem., Int. Ed.* **52**, 896 (2013), and related references therein
37. O. Sato, Y. Einaga, A. Fujishima, K. Hashimoto, *Inorg. Chem.* **38**, 4405 (1999)
38. Y. Ono, Doctoral Thesis, (The University of Tokyo, 2005)
39. S. Iijima, T. Katsura, H. Tamaki, M. Mitsumi, N. Matsumoto, H. Ôkawa, *Mol. Cryst. Liq. Cryst.* **233**, 263 (1993)
40. S. Iijima, F. Mizutani, M. Mitsumi, N. Matsumoto, H. Ôkawa, *Inorg. Chim. Acta* **253**, 47 (1996)
41. T. Birchall, K.M. Tun, *Inorg. Chem.* **15**, 376 (1976)
42. B.J. Evans, R.G. Johnson, F.E. Senftle, C.B. Cecil, F. Dulong, *Geochim. Cosmochim. Acta* **46**, 761 (1982)
43. T. Nakamoto, Y. Miyazaki, M. Itoi, Y. Ono, N. Kojima, M. Sorai, *Angew. Chem., Int. Ed.* **40**, 4716 (2001)
44. M. Enomoto, M. Itoi, Y. Ono, M. Okubo, N. Kojima, *Synth. Metals* **137**, 1231 (2003)
45. Y. Kobayashi, M. Itoi, N. Kojima, K. Asai, *J. Phys. Soc. Jpn.* **71**, 3016 (2002)
46. K. Nagamine, *Introductory Muon Science* (Cambridge University Press, 2003)
47. R.S. Hayano, Y.J. Uemura, J. Imazato, N. Nishida, T. Yamazaki, R. Kubo, *Phys. Rev. B* **20**, 850 (1979)
48. R. Kadono, T. Matsuzaki, T. Yamazaki, S.R. Kreitzman, J.H. Brewer, *Phys. Rev. B* **42**, 6515 (1990)
49. C.P. Slichter, *Principles of magnetic resonance* (Harper International, New York, 1965)
50. N. Kojima, N. Kida, A. Okazawa, M. Enomoto, *Mössbauer Eff. Ref. Data J.* **35**, 154 (2012)
51. H. Nakamichi, T. Okada, *Angew. Chem., Int. Ed.* **45**, 4270 (2006), and related references therein
52. R. Sessoli, D. Gatteschi, A. Caneschi, M.A. Novak, *Nature* **365**, 141 (1993)
53. T. Lis, *Acta Crystallogr. B* **36**, 2042 (1980)

54. A. Caneschi, D. Gatteschi, R. Sessoli, A.L. Barra, L.C. Brunel, M. Guillot, *J. Am. Chem. Soc.* **113**, 5873 (1991)
55. R. Sessoli, H.L. Tsai, A.R. Schake, S. Wang, J.B. Vincent, K. Folting, D. Gatteschi, G. Christou, D.N. Hendrickson, *J. Am. Chem. Soc.* **115**, 1804 (1993)
56. J.R. Friedman, M.P. Sarachik, J. Tejada, J. Maciejewski, R. Ziolo, *J. Appl. Phys.* **79**, 6031 (1996)
57. J.R. Friedman, M.P. Sarachik, J. Tejada, R. Ziolo, *Phys. Rev. Lett.* **76**, 3830 (1996)
58. L. Thomas, F. Lioni, R. Ballou, D. Gatteschi, R. Sessoli, B. Barbara, *Nature* **383**, 145 (1996)
59. T. Kuroda-Sowa, M. Lam, A.L. Rheingold, C. Frommen, W.M. Reiff, M. Nakano, J. Yoo, A.L. Maniero, L.-C. Brunel, G. Christou, D.N. Hendrickson, *Inorg. Chem.* **40**, 6469 (2001)
60. D. Gatteschi, R. Sessoli, A. Cornia, *Chem. Commun.* 725 (2000)
61. A.L. Barra, A. Caneschi, A. Cornia, F. Fabrizi de Biani, D. Gatteschi, C. Sangregorio, R. Sessoli, L. Sorace, *J. Am. Chem. Soc.* **121**, 5302 (1999)
62. C. Sangregorio, T. Ohm, C. Paulsen, R. Sessoli, D. Gatteschi, *Phys. Rev. Lett.* **78**, 4645 (1997)
63. A.L. Barra, P. Debrunner, D. Gatteschi, C.E. Schulz, R. Sessoli, *Europhys. Lett.* **35**, 133 (1996)
64. L. Cianchi, G. Spina, *Studies of spin fluctuations in single molecular magnets by using Mössbauer spectroscopy*, ed. by P. Carrette, A. Lascialfari, NMR-MRI,  $\mu$ SR and Mössbauer Spectroscopies in Molecular Magnets (Springer-Verlag, Milano, 2007)
65. C. Delfs, D. Gatteschi, L. Pardi, R. Sessoli, K. Wieghardt, D. Hanke, *Inorg. Chem.* **32**, 3099 (1993)
66. A. Cini, M. Mannini, F. Totti, M. Fittipaldi, G. Spina, A. Chumakov, R. Rüffer, A. Cornia, R. Sessoli, *Nat. Commun.* **9**, 480 (2018)
67. A.M. LaPointe, *Inorg. Chim. Acta* **345**, 359 (2003)
68. T. Viefhaus, W. Schwarz, K. Hübler, K. Locke, J. Weidlein, *Z. Anorg. Allg. Chem.* **627**, 715 (2001)
69. N.N. Greenwood, T.C. Gibb, *Mössbauer Spectroscopy* (Chapman and Hall, London, 1971)
70. W.M. Reiff, A.M. LaPointe, E.H. Witten, *J. Am. Chem. Soc.* **126**, 10206 (2004)
71. J.M. Zadrozny, M. Atanasov, A.M. Bryan, C.-Y. Lin, B.D. Rekker, P.P. Power, F. Neese, J.R. Long, *Chem. Sci.* **4**, 125 (2013)
72. J.M. Zadrozny, D.J. Xiao, J.R. Long, M. Atanasov, F. Neese, F. Grandjean, G.J. Long, *Inorg. Chem.* **52**, 13123 (2013)
73. S. Dattagupta, M. Blume, *Phys. Rev. B* **10**, 4540 (1974)
74. K.S. Cole, R.H. Cole, *J. Chem. Phys.* **9**, 341 (1941)
75. S.M.J. Aubin, Z. Sun, L. Pardi, J. Krzystek, K. Folting, L.-C. Brunel, A.L. Rheingold, G. Christou, D.N. Hendrickson, *Inorg. Chem.* **38**, 5329 (1999)
76. P.P. Power, *Chem. Rev.* **112**, 3482 (2012)
77. N.F. Chilton, H. Lei, A.M. Bryan, F. Grandjean, G.J. Long, P.P. Power, *Dalton Trans.* **44**, 11202 (2015)
78. S. Goda, M. Nikai, M. Ito, D. Hashizume, K. Tamao, A. Okazawa, N. Kojima, H. Fueno, K. Tanaka, Y. Kobayashi, T. Matsuo, *Chem. Lett.* **45**, 634 (2016)
79. A.M. Bryan, C.-Y. Lin, M. Sorai, Y. Miyazaki, H.M. Hoyt, A. Hablutzel, A. LaPointe, W.M. Reiff, P.P. Power, C.E. Schulz, *Inorg. Chem.* **53**, 12100 (2014)
80. W.M. Reiff, C.E. Schulz, M.-H. Whangbo, J.I. Seo, Y.S. Lee, G.R. Potratz, C.W. Spicer, G.S. Girolami, *J. Am. Chem. Soc.* **131**, 404 (2009)
81. W.A. Merrill, T.A. Stich, M. Brynda, G.J. Yeagle, J.C. Fettinger, R. De Hont, W.M. Reiff, C.E. Schulz, R.D. Britt, P.P. Power, *J. Am. Chem. Soc.* **131**, 12693 (2009)
82. T. Matsuo, K. Suzuki, T. Fukawa, B. Li, M. Ito, Y. Shoji, T. Otani, L. Li, M. Kobayashi, M. Hachiya, Y. Tahara, D. Hashizume, T. Fukunaga, A. Fukazawa, Y. Li, H. Tsuji, K. Tamao, *Bull. Chem. Soc. Jpn* **84**, 1178 (2011)
83. J.M. Zadrozny, D.J. Xiao, M. Atanasov, G.J. Long, F. Grandjean, F. Neese, J.R. Long, *Nat. Chem.* **5**, 577 (2013)
84. R.J. Glauber, *J. Math. Phys.* **4**, 294 (1963)
85. L. Bogani, A. Vindigni, R. Sessoli, D. Gatteschi, *J. Mater. Chem.* **18**, 4750 (2008)
86. W.-X. Zhang, R. Ishikawa, B. Breedlove, M. Yamashita, *RSC Adv.* **3**, 3772 (2013)

87. A. Caneschi, D. Gatteschi, N. Lalioti, C. Sangregorio, R. Sessoli, G. Venturi, A. Vindigni, A. Rettori, M.G. Pini, M.A. Novak, *Angew. Chem., Int. Ed.* **40**, 1760 (2001)
88. R. Clérac, H. Miyasaka, M. Yamashita, C. Coulon, *J. Am. Chem. Soc.* **124**, 12837 (2002)
89. C. Coulon, R. Clérac, L. Lecren, W. Wernsdorfer, H. Miyasaka, *Phys. Rev. B* **69**, 132408 (2004)
90. T. Kajiwara, M. Nakano, Y. Kaneko, S. Takaishi, T. Ito, M. Yamashita, A. Igashira-Kamiyama, H. Nojiri, Y. Ono, N. Kojima, *J. Am. Chem. Soc.* **127**, 10150 (2005)
91. T. Kajiwara, I. Watanabe, Y. Kaneko, S. Takaishi, M. Enomoto, N. Kojima, M. Yamashita, *J. Am. Chem. Soc.* **129**, 12360 (2007)